

Article

Not peer-reviewed version

---

# Nano-indentation Response of Structural Self-Healing Epoxy Resin: A Hybrid Experimental-Simulation Approach

---

Giovanni Spinelli<sup>\*</sup>, Rosella Guarini, [Evgeni Ivanov](#), [Elisa Calabrese](#), [MariaLuigia Raimondo](#), [Raffaele Longo](#), [Liberata Guadagno](#)<sup>\*</sup>, [Luigi Vertuccio](#)

Posted Date: 3 June 2024

doi: 10.20944/preprints202406.0112.v1

Keywords: nano-indentation; epoxy resin; mechanical properties; self-healing



Preprints.org is a free multidiscipline platform providing preprint service that is dedicated to making early versions of research outputs permanently available and citable. Preprints posted at Preprints.org appear in Web of Science, Crossref, Google Scholar, Scilit, Europe PMC.

Copyright: This is an open access article distributed under the Creative Commons Attribution License which permits unrestricted use, distribution, and reproduction in any medium, provided the original work is properly cited.

*Article*

# Nano-Indentation Response of Structural Self-Healing Epoxy Resin: A Hybrid Experimental-Simulation Approach

Giovanni Spinelli <sup>1,2,\*</sup>, Rosella Guarini <sup>2,3</sup>, Evgeni Ivanov <sup>2,4</sup>, Elisa Calabrese <sup>3</sup>,  
Marialuigia Raimondo <sup>3</sup>, Raffaele Longo <sup>3</sup>, Liberata Guadagno <sup>3,\*</sup> and Luigi Vertuccio <sup>5</sup>

<sup>1</sup> Faculty of Transport Sciences and Technologies, University of Study "Giustino Fortunato",  
Via Raffaele Delcogliano 12, 82100 Benevento, Italy

<sup>2</sup> Open Laboratory on Experimental Micro and Nano Mechanics, Institute of Mechanics, Bulgarian Academy  
of Sciences, Acad. G. Bonchev Str., Block 4, 1113 Sofia, Bulgaria; rgrosagi@gmail.com (R.G.);  
ivanov\_evgeni@yahoo.com (E.I.)

<sup>3</sup> Department of Industrial Engineering, University of Salerno, Via Giovanni Paolo II, 84084 Fisciano, Italy;  
elicalabrese@unisa.it (E.C.), mraimondo@unisa.it (M.R.), rlongo@unisa.it (R.L.)

<sup>4</sup> Research and Development of Nanomaterials and Nanotechnologies, NanoTech Lab Ltd.,  
Acad. G. Bonchev Str., Block 4, 1113 Sofia, Bulgaria

<sup>5</sup> University of Campania "Luigi Vanvitelli", Via Roma 29, 81031 Aversa, Italy;  
luigi.vertuccio@unicampania.it

\* Correspondence: g.spinelli1@unifortunato.eu (G.S.); lguadagno@unisa.it (L.G.)

**Abstract:** In these last years, self-healing polymers have emerged as a topic of considerable interest owing to their capability to partially restore material properties and thereby extend the product's lifespan. The main purpose of this study is to investigate the nano-indentation response in terms of hardness, reduced modulus, contact depth and coefficient of friction of a self-healing resin developed for use in aeronautical and aerospace contexts. To achieve this, the bifunctional epoxy precursor underwent tailored functionalization to improve its toughness, facilitating effective compatibilization with a rubber phase dispersed within the host epoxy resin. This approach aimed to highlight the significant impact of the quantity and distribution of rubber domains within the resin on enhancing its mechanical properties. The main results are that pure resin exhibits a higher hardness (about 36.7% more) and reduced modulus (about 7% more), consequently leading to a lower contact depth and coefficient of friction (11.4% less) compared to other formulations that, conversely, are well-suited for preserving damage from mechanical stresses due to their capabilities in absorbing mechanical energy. Furthermore, finite element method (FEM) simulations of the nanoindentation process were conducted. The numerical results were meticulously compared with experimental data, demonstrating a good agreement. This validation of the FEM model underscores its efficacy in predicting the mechanical behavior of nanocomposite materials under nanoindentation. The proposed investigation aims to contribute knowledge and optimization tips about self-healing resins.

**Keywords:** nano-indentation; epoxy resin; mechanical properties; self-healing

## 1. Introduction

In recent years, polymers with different functional properties have increased the interest of the industrial and academic community [1–6]. In particular, self-healing polymers have garnered significant attention due to their ability to partially or totally restore material properties, thereby extending product lifespans. Additional advantages include minimizing the environmental footprint and reducing resource depletion [7–10]. The self-repair process may occur autonomously or with external assistance, yet it is invariably initiated by damage to the material.

Previous research on self-healing polymeric materials has yielded numerous healing mechanisms, with current efforts increasingly directed toward developing advanced systems capable of supporting multiple healing cycles [11–13]. Thermosetting polymers, especially epoxies, are extensively used in coatings, adhesives, and structural components due to their high mechanical strength, thermal stability, and resistance to chemicals and corrosion [14,15]. However, their highly crosslinked network limits intrinsic healing mechanisms [16]. Modifications to epoxies aim to enhance healing functionality, with various strategies reported in literature considering that self-healing polymers can be classified as either extrinsic or intrinsic [17]. Extrinsic polymers rely on auto-repair mechanisms that involve external healing agents stored typically in the form of microcapsules or vascular channels, which are discharged to seal the areas of damage. Upon damage occurrence and propagation within the material, these reparative substances rupture, thus initiating with the support of a suitable catalyst the self-healing process and resulting in localized repair [18]. Researchers have successfully applied this strategy to impart self-healing properties to epoxy resins modified with carboxyl-terminated butadiene acrylonitrile (CTBN) rubber for adhesive applications [19].

On the other hand, intrinsic self-healing polymers utilize reversible bonds, including dynamic covalent and noncovalent bonds present within the material, to restore the polymer's integrity after damage occurs [20]. Compared to capsule-based and vascular self-healing materials, intrinsic self-healing materials are simpler and alleviate challenges associated with integrating healing agents, ensuring compatibility, and maintaining catalyst stability [21]. Nevertheless, many intrinsic self-healing systems lack mechanical and chemical properties suitable for structural applications. Hence, epoxies, renowned for their suitability in such applications, are modified to enhance mechanical properties combined with efficient healing capabilities. Different studies in the literature are focused on these objectives. Outwater *et al.* proposed a novel method to measure the fracture energy of cast epoxy resin in the presence of different agents [22]. In this pioneering work, it is observed that upon heating above the glass transition temperature ( $T_g$ ), the crack spontaneously healed, resulting in a fresh joint with a fracture energy comparable to that of the original material. The authors attributed this phenomenon to micro-Brownian motions facilitating the local flow and ensuring sound bond formation [22]. Likewise, Rahmathullah *et al.* implemented a healing protocol for addressing an arrested crack within fully cured epoxy-amine thermosets [23]. Several studies reported that the explanation for the superficial repair of epoxy cracks involves shape-memory mechanisms. Luo and Mather presented the preparation and characterization of novel shape memory-assisted self-healing (SMASH) coatings [24]. These coatings exhibit a phase-separated morphology of electrospun thermoplastic poly( $\epsilon$ -caprolactone) (PCL) fibers, dispersed randomly within a shape memory epoxy matrix. [24]. Nelson *et al.* reported a temperature-dependent recovery of atomic force microscope tip-formed indentations in a thermoset shape memory polymer, highlighting with their study that the shape recovery is more complete for higher anneal temperature [25]. Cho *et al.* investigated self-healing polymer coatings to study the differences in using two distinct approaches: first, the catalyst is microencapsulated in the epoxy resin, whereas the healing agent (siloxanes) was as phase-separated droplets. In the second approach, both phases were also encapsulated and dispersed in the coating matrix. As a result, it was found that this second solution appears valuable in cases where the matrix can react with the healing agent [26]. Our previous studies showed an intrinsic self-healing system comprising an epoxy resin covalently modified with a rubber phase and self-healing fillers dispersed in the epoxy system. [27,28]. Incorporating the elastomer component decreases the rigidity of the epoxy chains and stimulates the activation of an auto-repair mechanism driven by hydrogen bonding interactions. Moreover, rubber-enhanced thermosetting resins demonstrate several advantages over their unmodified counterparts. In a previous paper [29], the authors examined the influence of the functionalization temperature (120°C and 160°C,) to obtain an efficient toughened material. In particular, FT/IR and DMA analyses were used to investigate the functionalization of the epoxy precursor with the elastomeric phase at two different temperatures. The results showed a higher fraction of rubber phase bonded to the epoxy precursor at the higher functionalization temperature of 160 °C compared to 120 °C. Moreover, self-healing tests via tapered double cantilever beam (TDCB) also demonstrated a significant healing efficiency for the system functionalized at 160

°C compared to that at 120 °C. In the present work, the nanocomposites obtained through a functionalization temperature of 160°C were further characterized by nanoindentation tests in terms of hardness, reduced modulus, contact depth, and coefficient of friction (COF) at scratch.

Microstructural analysis and nanoindentation characterization are recently generating increasing interest to further explore mechanical properties at the nanoscale level [30].

The nanoindentation technique is successfully presented in literature to study the creep behavior of supercrystalline nanocomposites (SCNCs) with different levels of organic crosslinking[31].

The improvement of mechanical properties in terms of elastic modulus due to the incorporation of nanoclay platelets into epoxy resin has been also analyzed via nanoindentation [32].

The innovative method based on accelerated property mapping (XPM), which provides measuring maps of local mechanical properties (reduced modulus, hardness), it is also employed in the current investigation. All observed results are compared with those related to the unmodified hosting epoxy resin adopted as a reference.

Finally, finite element simulation studies are undertaken to predict additional mechanical properties of the formulated samples, leveraging select experimental results.

This experimental/computational hybrid approach has been successfully presented in the literature to introduce and support laboratory tests concerning the nanoindentation of heterogeneous nanocomposite materials [33]. Similarly, mathematical approaches have been proposed to interpret the results of nanoindentation characterization concerning the elastic and viscoelastic properties of polymer nanocomposites [34].

## 2. Materials

### 2.1. Materials

Although the samples are part of a broader set of composites investigated differently in a previous study [29], their preparation is recalled here for clarity and completeness.

The prepared samples consist of a toughened epoxy matrix including the precursor (Gurit Holding, Wattwil, Switzerland) "3,4-Epoxy cyclohexylmethyl-3',4'-epoxycyclohexane carboxylate" (acronyms ECC and chemical formula  $C_{14}H_{20}O_4$ ) and the hardener agent (Gurit Holding, Wattwil, Switzerland) "Methylhexahydrophthalicanhydride" (acronyms MHHPA and chemical formula  $C_9H_{12}O_3$ ) in a 1:1 ratio.

The liquid rubber that acts as a toughening agent, Carboxyl-Terminated Butadiene Acrylonitrile Copolymer (henceforth designed as "R"), was used at a concentration of 5 wt% with respect to the overall mixture. It was supplied by Hycar-Reactive Liquid Polymers, featuring a molecular weight ( $M_n$ ) of 3600, and containing terminal carboxy groups (with a COOH content of  $0.67 \times 10^{-3}$  equiv/g of CTBN and 18 w/w% of CN). The catalyst, triphenylphosphine (PPh<sub>3</sub>, Merck KGaA, Darmstadt, Germany), was added to facilitate the functionalization reaction of the epoxy precursor (ECC).

Figure 1 reports (from left to right,) the chemical structures of the following components: epoxy precursor (ECC), liquid rubber (R) and hardener (MHHPA) respectively, whereas Table S1 of section "Supplementary electronic materials (S.E.M.)" summarizes the quantities in grams and percentages of individual components required to produce 23.58 g of the complete mixture, here named Ep-R-160.

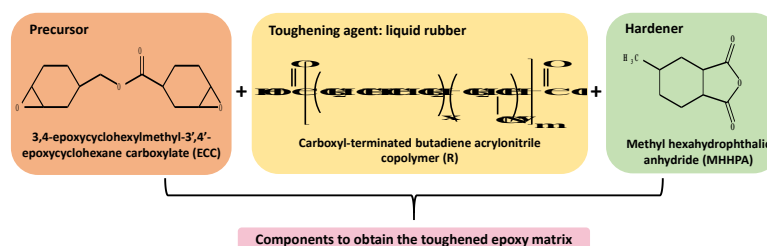


**Figure 1.** Chemical details of the precursor, hardener agent and toughening agent, from left to right, respectively.



Based on the selected composition, the initial nucleophilic attack through triphenylphosphine unlocks  $9.15 \times 10^{-3}$  mol of oxirane rings, thus leaving still unreacted  $7.0 \times 10^{-2}$  mol of oxirane rings, which represent the 88% of the rings initially present. The moles of the terminal carboxylic groups are equivalent to  $0.804 \times 10^{-3}$  which result a quantity slightly lower than the opened oxirane rings ( $9.15 \times 10^{-3}$  mol).

This decision was taken to prevent the formation of extensive elastomeric domains within the resin, as later confirmed through SEM analysis. Drawing from both previously published research [35] and the expertise of the authors, it was observed that a reduction in triphenylphosphine content (or an increase in the rubber phase relative to the amount of PPh<sub>3</sub>) leads to larger elastomer domains, resulting in significant local inhomogeneity on the scale of hundreds or thousands of microns.

The self-healing additives, with chemical structures depicted in Figure 2, 1,3-Dimethylbarbituric acid (DBA), 2-Thiohydantoin (T), and Murexide (M) (all sourced from Merck KGaA, Darmstadt, Germany) were included at a concentration of 0.42 wt%. The capacity of these additives to initiate self-repair mechanisms through hydrogen bonding interactions has been previously established. This was demonstrated in prior research utilizing a nano-enhanced resin composed of a tetra-functional epoxy precursor cured with 4,4-diamino diphenyl sulfone [27].

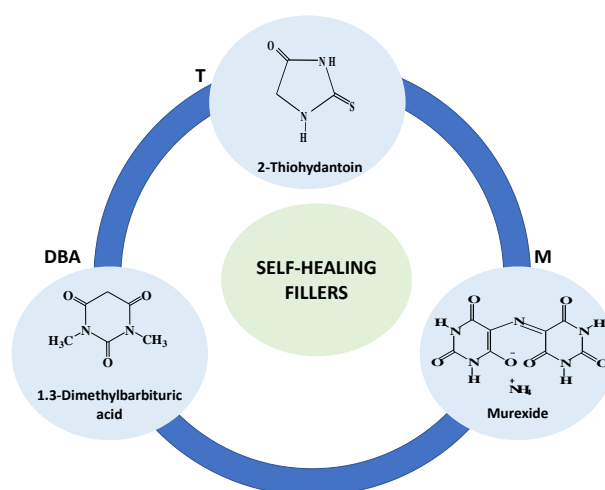


**Figure 2.** Chemical structure of molecules acting as self-healing filler.

## 2.2. Formulation of Epoxy Sample

### 2.2.1. Functionalized Epoxy Precursor

The ECC-R-160 functionalized precursor liquid blends consisted of epoxy precursor molecules chemically modified with the rubber phase. These blends were prepared by mechanically stirring a mixture of ECC epoxy precursor, elastomer R, and PPh<sub>3</sub> catalyst for 15 hours at a temperature of 160°C.

### 2.2.2. Functionalized Epoxy Samples

The cured epoxy samples, labeled as Ep-R-160, were prepared by adding the hardener MHHPA to the functionalized precursor ECC-R-160 using magnetic stirring for 20 minutes at room temperature. After degassing for 2 hours at room temperature, the mixture underwent polymerization in an oven through a curing cycle comprising 1 hour at 80°C, followed by 20 minutes at 120°C, and then 1 hour at 180°C. During the curing process, the samples were initially placed in the oven at 80°C. After the first hour of curing, the oven temperature was ramped from 80°C to 120°C at a rate of 10°C/min, while the actual heating rate measured with a probe was 4°C/min. The same procedure was followed for the transition from 120°C to 180°C. For comparison, an EP sample, representing the cured epoxy matrix without the rubber phase, was prepared by mixing the ECC

precursor and MHPA hardener, following the aforementioned procedure. Functionalized epoxy samples containing the selected molecules (DBA, T, and M), as depicted in Figure 2, were obtained by dispersing the self-healing filler into the functionalized precursor ECC-R-160 using ultrasonication for 30 minutes at room temperature. Subsequently, the addition of the hardener and the curing cycle were conducted following the same procedure described earlier. The resulting samples were labeled as Ep-R-160-DBA, Ep-R-160-T, and Ep-R-160-M.

### 2.3. Morphological Analysis by Scanning Electron Microscope (SEM)

Scanning electron microscope (SEM) micrographs to analyze the morphology in terms of dimensions and dispersal state of the rubber domains in the hosting epoxy resin, were captured using a field emission SEM apparatus (JSM-6700F, Jeol, Akishima, Japan) operating at 3 kV. Sections of the composites were obtained by cutting solid samples using a sledge microtome. These sections were etched and then gold-sputtered before SEM observation, by following a procedure, already detailed in Spinelli *et al.* [36] and in Guadagno *et al.* [37]

### 2.4. Nano-Indentation Tests

To evaluate the mechanical properties, nanoindentation tests, accelerated property mapping (XPM) and nanoscratch assessments were conducted using (see Figure 3) a Hysitron TI 980 instrument (Bruker, Billerica, MA, USA) by using a 2D transducer assembly (both normal and lateral force) equipped with a Berkovich probe.

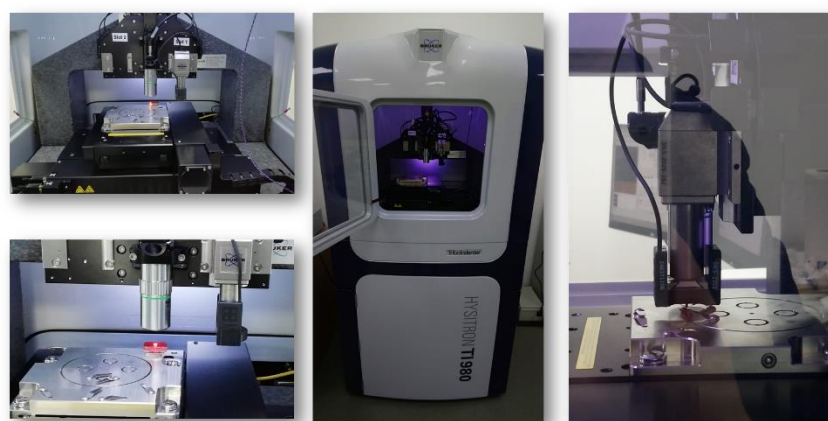


**Figure 3.** Nanomechanical test system for innovative material characterization.

A standard Berkovich indenter typically has a radius of curvature of approximately 150 nm. Tip-area calibration was performed using a standard fused quartz specimen with a notorious elastic modulus (69.6 GPa).

A load control mode was selected for the nanoindentation test, which was conducted applying a trapezoidal load function with a peak force of 8.000  $\mu\text{N}$  (refer to the next section Results for details about slopes and durations) whereas, nanoscratch experiments involved the application of a constant load scratch function with a maximum force set at 1500 Newtons.

Each test involved 49 indents (arranged in a 7  $\times$  7 grid; indent spacing 10  $\mu\text{m}$ , see Figure 4) to collect statistical data and limit load-displacement curve variability due to not perfectly smooth surfaces of the specimens.

Generally, the XPM testing method follows the same procedure as the standard nanoindentation technique but is expedited by shortening the duration of the functional segments.

In particular, the XPM analysis was performed on a sample surface area measuring 70  $\times$  70 micrometers, nearing the upper limit of the piezo scanner's range. Accelerated property mapping

was executed utilizing a trapezoidal load function characterized by brief loading, holding, and unloading intervals, each lasting a fraction of a second.

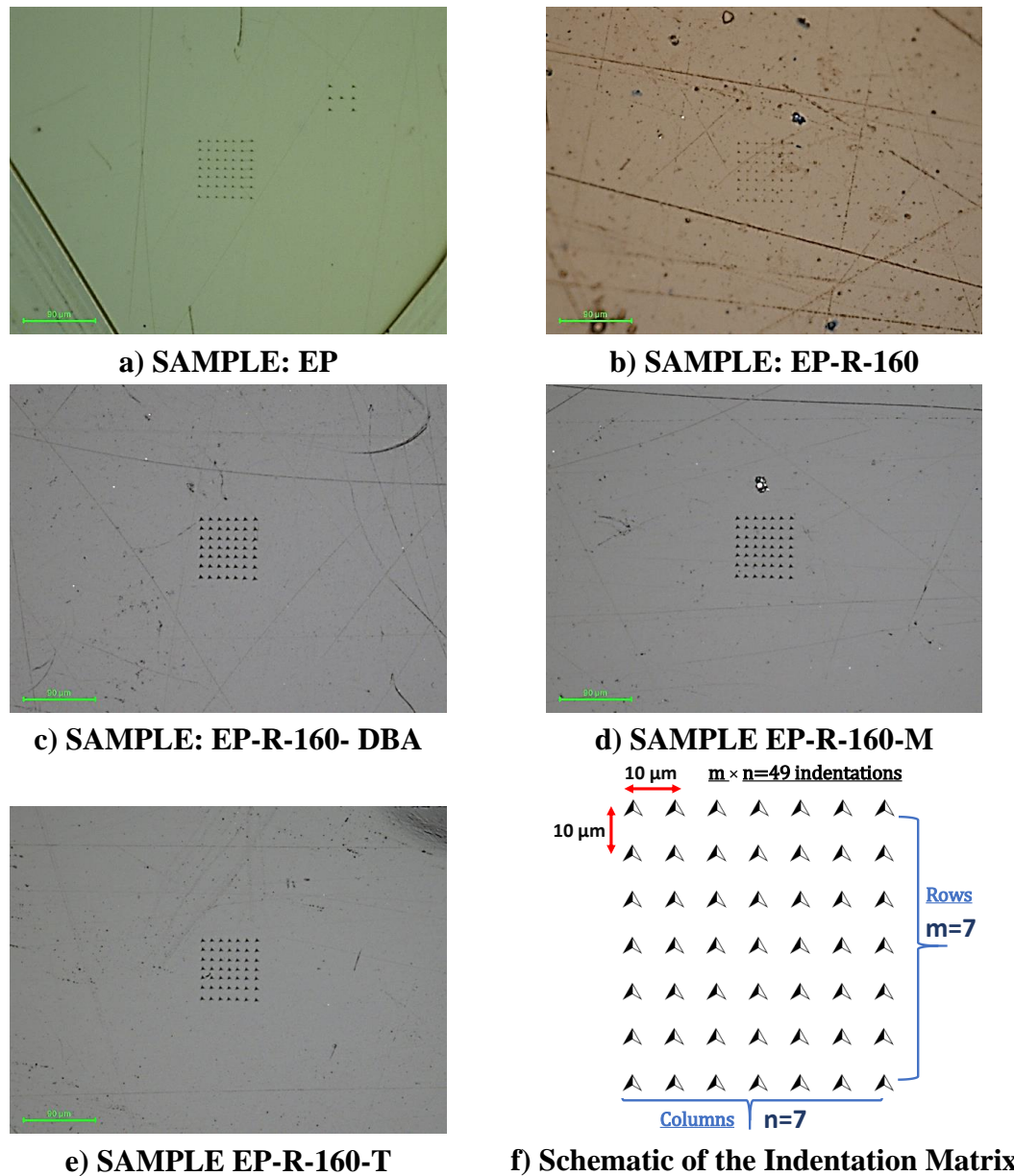
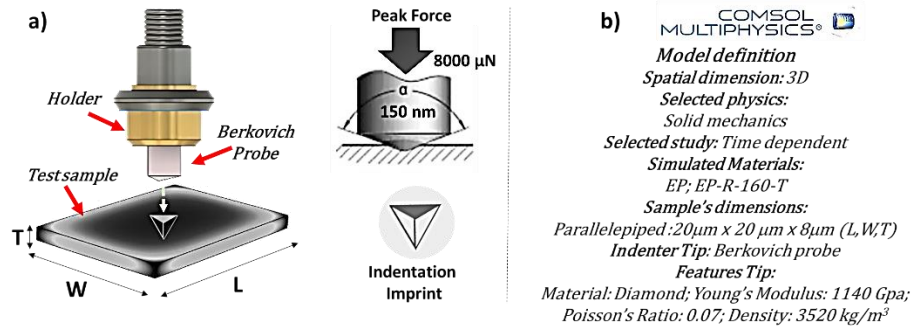


**Figure 4.** Optical images of XPM nanoindentation test trace made on the surface of a) EP-R ; b) EP-R-160; c) EP-R-160-DBA; d) EP-R-160-M, and e) EP-R-160-T. Schematic representation of the indentation matrix in f).

## 2.5. Multiphysic Simulation Study of Naomechanical Properties

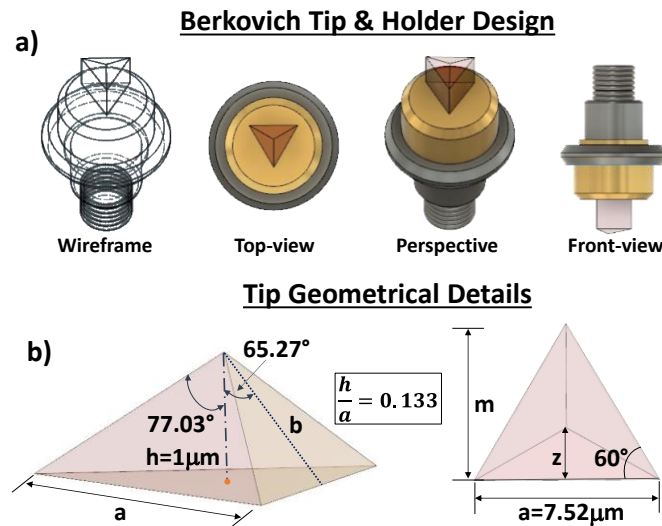
In this study, the nanomechanical behavior in terms of local displacement, hardness and Von Mises stress of some selected composites was examined through numerical analysis based on 3D finite element method (FEM). COMSOL Multiphysics® (version 6.1) served as the simulation environment, in which the experimentally Berkovich's tip used for the experimental nanomechanical characterization was faithfully replicated. It is designed with a 3D cad software (FUSION 360) according to the general information reported on the manufacturer's data sheet, and then imported in COMSOL. This because the shape of the indenter is recognized as remarkable parameter conditioning the results and insights of nanoindentation tests [38]. Therefore, the authors' efforts were concentrated on overcoming the limitations of other literature tip models commonly used for indentation modeling, which are typically based on sphero-conical or triangular geometries [39–41].

Figure 5 a) and Figure 5 b) provide a schematic depiction of the considered case study and the essential model definitions selected for the simulations, respectively.



**Figure 5.** (a) Graphic illustration of the simulated case study. (b) Crucial model definitions selected for the numerical analysis.

Given the importance and the role that it plays in simulations results, further details about the indenter tip are reported in Figure 6 which shows some different views of the Berkovich probe in a) and its geometrical feature in b).



**Figure 6.** Cad images in a) and geometrical details of the Berkovich's indenter tip in b).

With reference to the geometrical details shown in Figure 6 b), below are the straightforward mathematical steps necessary to determine the projected contact area (hereafter,  $A_{proj}$ ) as a function of the indentation depth ( $h_i = h \cdot c$  with  $c$  real coefficient varying in the range  $[0, \approx 1]$ ) between the material and the tip, i.e.  $A_{proj} = f(h_i)$ .

By considering the following relationships:

$$\tan 60^\circ = \frac{m}{a/2}; \quad m = \frac{\sqrt{3}}{2} a; \quad \cos 65.27^\circ = \frac{h_i}{b} \quad (1)$$

the projected contact area  $A_{proj}$  can be calculated according to the following expression:

$$A_{proj} = \frac{a \cdot m}{2} = \frac{\sqrt{3}}{4} a^2. \quad (2)$$

Taking into account the relationship:

$$h_i = \frac{a \cdot \cos 65.27^\circ}{2\sqrt{3} \sin 65.27^\circ} = \frac{a}{2\sqrt{3} \tan 65.27^\circ} \quad (3)$$

the projected contact area  $A_{proj}$  assumes the final expression, as a function of the indentation depth ( $h_i$ ), in the form:

$$A_{proj} = 3\sqrt{3} h_i^2 \tan^2 65.27^\circ \cong 24.56 \cdot h_i^2 \quad (4)$$



This parameter is crucial for numerically estimating the material's hardness (H). In fact, the hardness is determined from the maximum load ( $L_{max}$ ), divided by the projected contact surface, according to the Doerner-Nix model expressed by the following equation [42]:

$$H = \frac{L_{max}}{A_{proj}} \quad (5)$$

### 3. Results

The mechanical characteristics of a material rank among the foremost considerations when designing a structural component. Nanoindentation is a widely recognized technique for assessing mechanical properties at the nanoscale, achieved by tracking displacements of a calibrated indenter tip into a specimen's surface while applying forces. The resultant force-displacement curve facilitates the derivation of material properties such as elastic modulus and hardness, employing methodologies like the Oliver and Pharr method [43], as well as other interesting mechanical properties investigated in the next subsections which are strictly correlated to the morphological analysis conducted preventively.

#### 3.1. Morphological Investigation

Figure 7 shows the SEM images of the samples EP-R-160-DBA (Figure 7a), EP-R-160-M (Figure 7b), and EP-R-160-T (Figure 7c). All three images show a rubber phase in the form of small globular domains well anchored to the hosting matrix, as a proof of a successful functionalization. The globular domains of the elastomeric phase are characterized by roughly the same dimensions for all samples. The average globular domains' diameter ranges between 314 nm (for EP-R-160-DBA sample) to 354 nm (for EP-R-160-M sample) and 397 nm (for EP-R-160-T sample). As shown in Figs 7d, 7e, and 7f, a monomodal distribution is detected for all samples. Rubber domain diameter distribution was calculated according to a procedure already described in a previous paper [44]. The statistical investigation involved the analysis of over 200 elastomeric domains.

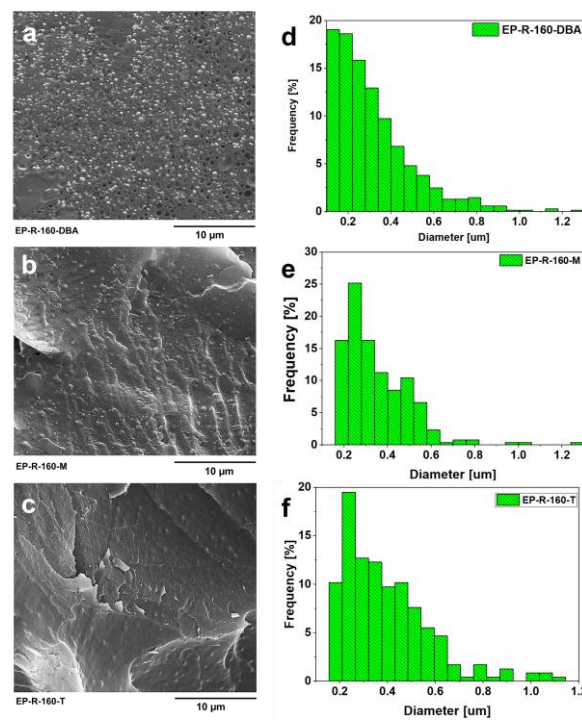


**Figure 7.** SEM images of the samples EP-R-160-DBA (Figure 7a), EP-R-160-M (Figure 7b), and EP-R-160-T (Figure 7c); rubber domains diameter distribution of EP-R-160-DBA (Figure 7d), EP-R-160-M (Figure 7e), and EP-R-160-T (Figure 7f).

### 3.2. Quasi-Static Nano-Indentation

In an initial experimental investigation aimed at surface characterization of nanocomposite materials, a nanoscale indentation following the Oliver-Pharr method [43] is adopted to evaluate the hardness (H) and reduced elastic modulus ( $E_r$ ) of the samples as well as the respective contact depth and the coefficient of friction (COF) at scratch. In particular, the nanoindentation hardness is determined by dividing the peak load ( $P_{\max}$ ) by the contact area of the indenter (A), whereas the process for calculating the reduced modulus of elasticity entails fitting the unloading section of the load-displacement curve with a power-law function to ascertain stiffness. Subsequently,  $E_r$  is estimated by establishing the mathematical relationship between unloading stiffness and the projected contact area under load. Notably, this calculation considers elastic deformations in the specimen and the indenter. Indeed, reduced modulus ( $E_r$ ) in the nanoindentation test is determined using the Sneddon's formula [45]:

$$\frac{1}{E_r} = \frac{(1 - \nu^2)}{E} + \frac{(1 - \nu_i^2)}{E_i} \quad (1)$$

where E and  $\nu$  represent the elasticity modulus and Poisson's ratio of the test specimen, while  $E_i$  and  $\nu_i$  denote the elasticity modulus and Poisson's ratio of the indenter tip.

The experimental results of aforementioned mechanical properties are graphically reported in Figure 8 a), b), c) and d) respectively, whereas all numerical results, including statistical information, are summarized in Table S2 of section E.S.M.

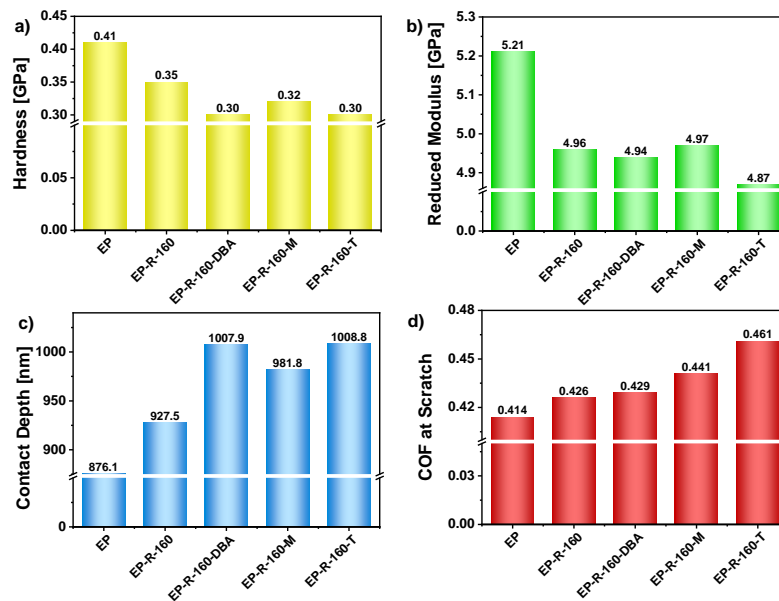


**Figure 8.** Hardness (a), reduced modulus (b) and contact depth (c) obtained after the XPM nanoindentation at the max force of 8000 uN; Coefficient of friction (COF) at scratch (d), after nanoscratch at 1500 uN constant load.

The findings presented in this study reveal that the hardness of sample EP exhibits an approximately 36.7% increase when compared to samples EP-R-160-DBA and EP-R-160-T (see Figure 8a). The unfunctionalized unfilled epoxy resin (EP sample) tends to be harder than rubber-functionalized epoxy due to its higher cross-linking density and the absence of a rubber phase, which reduces the matrix's rigidity. The addition of finely well-dispersed globular domains of rubber acting as a plasticizer reduces the overall hardness.

Rubber-functionalized epoxy with self-healing fillers shows a phase composition with nanodispersions domains (as highlighted by the SEM investigation) causing localized deformation and further reducing hardness.

On the other hand, the same observations just reported can justify the results regarding the reduced modulus (see Figure 8 b) of the sample EP, which is about 7% higher compared with the other samples. As a consequence of this higher stiffness of the not functionalized epoxy matrix (EP sample) with respect to the remaining samples analyzed, and as evident from the Figure 8 c), the contact depth for it is significantly lower (876.1 nm) in comparison with the other measured values. Finally, regarding the coefficient of friction (COF) during scratch testing reported in Figure 8 d), sample EP-R-160-T demonstrates the highest coefficient, showing an enhancement of approximately 11.4% and 8.2% compared to sample EP and EP-R-160, respectively.

This enhancement in scratch resistance can be attributed to the incorporation of rubber domains, which alter the material's mechanical properties and enhances its ability to withstand external forces in lateral displacements.

In particular, in the rubber-functionalized epoxy, the dispersed rubber phase acts as energy-dissipating regions upon scratching. These rubber domains can absorb and distribute the applied force, reducing the severity of scratches and preventing crack propagation. To complete this analysis, Figure 9 shows the time evolution of the of friction during scratching (defined as the ratio between the lateral force LF and normal force NF) for these two mechanically opposing formulations considered in this study, i.e., the unmodified resin (EP) and the EP-R-160-T sample in a) and b), respectively.

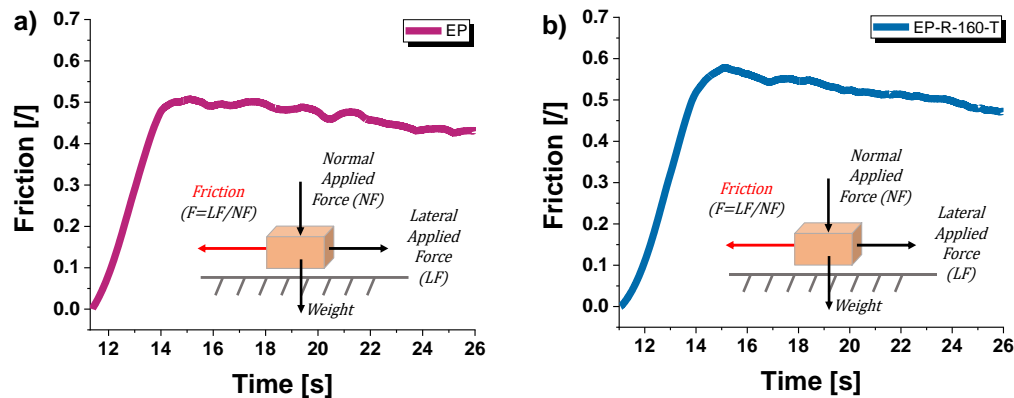


**Figure 9.** Friction (LF/NF) over time at scratch for a) EP-R and b) EP-R-160-T samples.

It is worth noting that, in line with the previously mentioned considerations, the EP-R-160-T sample exhibited greater resistance over time to the strain caused by the indenter scratching movement than the EP sample.

Figure 10 displays average load-displacement curves (from 49 tests), depicting different levels of indenter penetration within the composite samples (see Figure 10 b).

Applying a trapezoidal load function with a maximum force of 8000  $\mu\text{N}$  (see Figure 10a) led to a deeper displacement exceeding 700 nm within the material, thereby enabling a more comprehensive assessment of the combined effects on elastic modulus and hardness. The reduced maximum displacement observed in the curves corresponding to the EP sample indicates greater resistance to indenter movement within the material.

This suggests, once again, that this composite has higher mechanical properties, particularly in terms of stiffness, compared to those containing rubber domains (the remaining composites investigated).

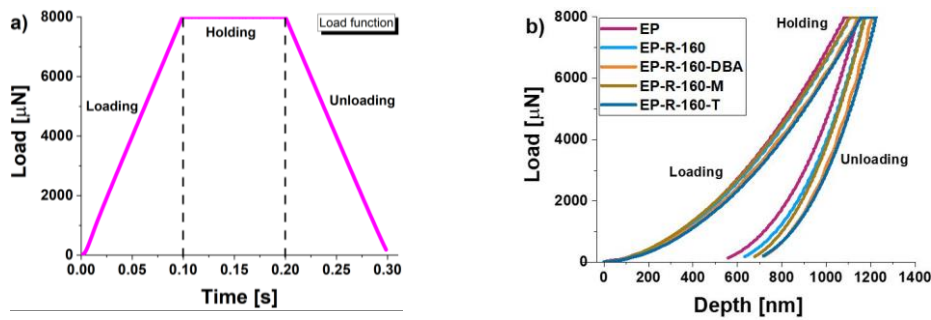


**Figure 10.** Trapezoidal load function applied for the nanomechanical characterization in a); Force vs displacement curves after accelerated nanomechanical property mapping XPM of all investigated samples in b).

It is interesting to note how the results from nanomechanical characterization align with the experimental findings of Dynamic Mechanical Analysis (DMA) conducted in our previous study [29] and hereafter referenced for clarity and ease of comparison (see Figure 11 which reports the Tan  $\delta$  and storage modulus vs temperature for unmodified (EP) and rubber functionalized (EP-R-160) samples, in a) and b), respectively.

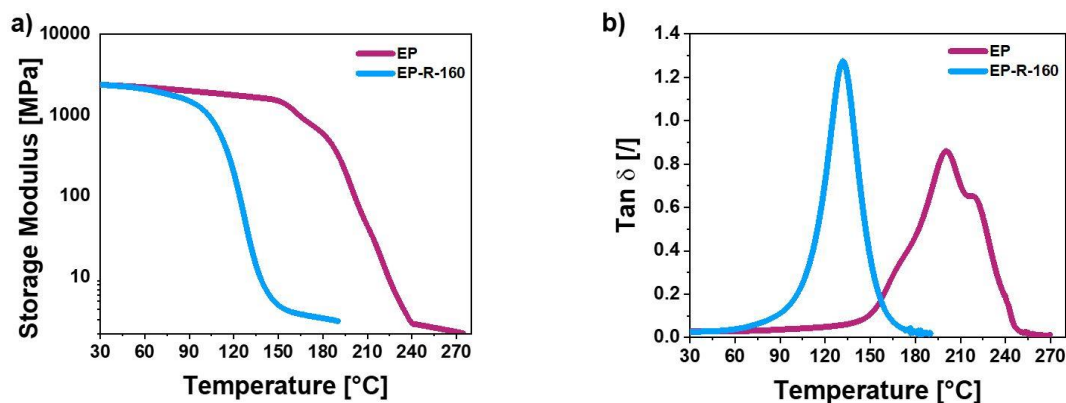


**Figure 11.** DMA curves for not modified epoxy sample (EP) and rubber functionalized specimen (EP-R-160): a) Tan  $\delta$  vs. temperature; b) Storage modulus vs. temperature.

The sample of unmodified resin (EP), which exhibited higher values of hardness and reduced modulus compared to those functionalized with rubber, showed the highest peak in the mechanical spectrum, related to the glass transition (i.e.,  $T_g$ ), which is centered at 200  $^{\circ}\text{C}$ , whereas for the rubber-functionalized sample (EP-R-160), it appears around 132  $^{\circ}\text{C}$ . Furthermore, it is noticeable that the introduction of rubber also affects the storage modulus. The primary decrease in the storage modulus occurs at lower temperature values for EP-R-160 as a result of incorporating the functionalized precursor into the resin. This is a very relevant result. In fact, a big challenge addressed in the formulation of these self-healing resins was to improve the resin's dynamic properties and reduce the matrix's rigidity, acting on its phase composition. Therefore, the design of a material with small domains of the polymer (rubber phase) at higher mobility, finely interpenetrated in the resin, has allowed higher mobility of the chains around the elastomeric domains, and a higher efficiency in the autorepair action. DMA analysis evidences a reduction of the rigidity of the matrix (at the macroscopic level), as evidenced before by the results of "Quasi-static nano-indentation" tests. In Figure 11 it is clearly visible that the peak of Tan  $\delta$  vs. temperature, for the sample containing rubber phase, opens around 60  $^{\circ}\text{C}$ . This peak is shifted to a lower temperature range with respect to the sample without rubber phase. It involves a temperature range from 60  $^{\circ}\text{C}$  to 180  $^{\circ}\text{C}$  (with a max around 132  $^{\circ}\text{C}$ ), where the sample without the rubber phase shows a transition from 140  $^{\circ}\text{C}$  to 250  $^{\circ}\text{C}$ .

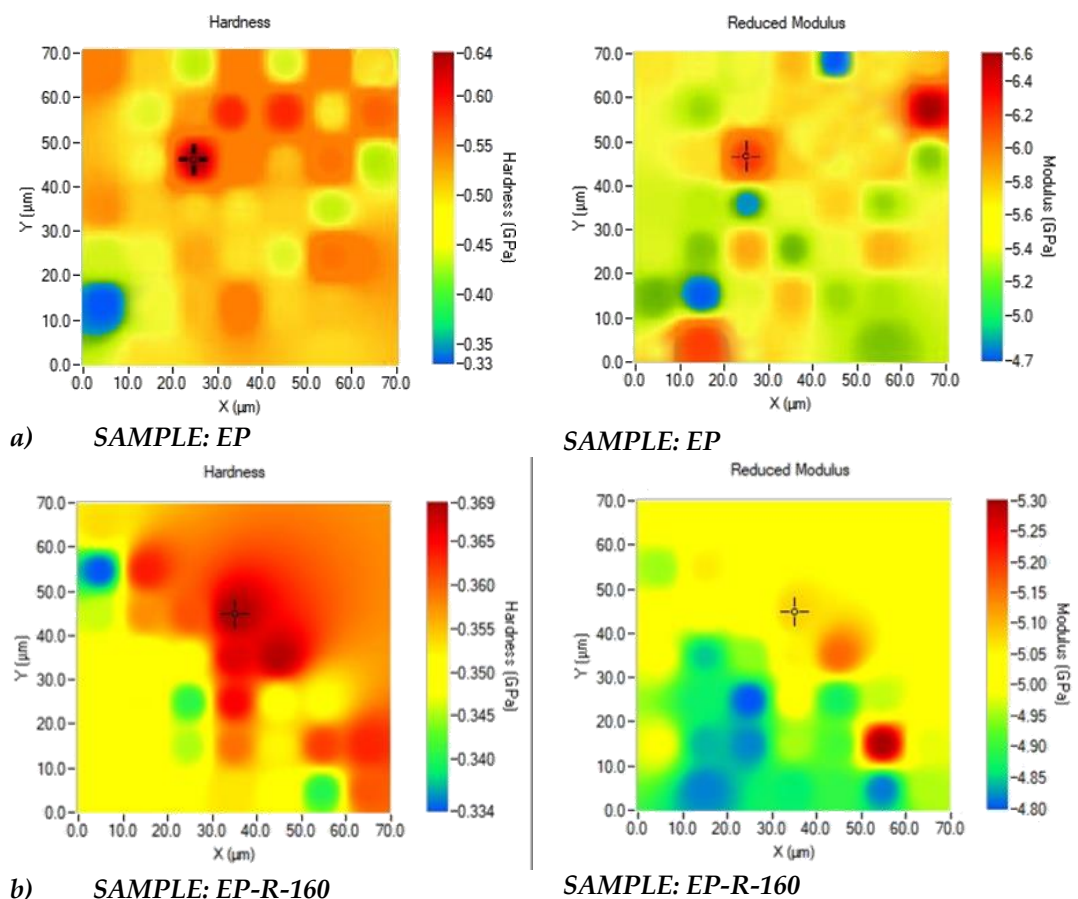


### 3.3. Accelerated Property Mapping (XPM) Investigation

To understand the mechanical behavior of multiphase materials, it is essential to determine the properties of individual phases and their interactions at the nano- and microscale. Advances in nanoindentation, especially the XPM (rapid indentation) technique, have significantly reduced testing times. XPM, combined with high-resolution microscopy, allows for visualizing hardness and modulus distribution across a sample [46]. It employs a piezo scanner for rapid positioning, creating a grid-like process and generating contour maps of the composite sample. Figure 12 shows the hardness (left parts of the figure) and reduced modulus (right parts) maps determined from the XPM test performed on all formulations considered in the present work. Distinct colors indicate varying levels of the two aforementioned mechanical properties.

Irrespective of the hardness and elastic modulus levels, as indicated by the color bar on the right side of each XPM map, surface mechanical characteristics appear consistent across all samples, particularly for the non-functionalized epoxy resin (see Figure 12 a).

This specific composite demonstrates the most homogeneous surface properties compared to the other remaining XPM images which show, in any case, a good uniformity of surface hardness and reduced modulus, as illustrated in Figure 12 (b-e). These results further validate the authors' meticulous selection of the chemical composition outlined in the Materials section to prevent the formation of big domains of the elastomeric phase within the resin, thus mitigating observable local inhomogeneity. An overview of the hardness and reduced elastic modulus data obtained from XPM testing suggests minimal contrast compared to values derived from quasi-static nanoindentation. This lack of contrast may be attributed to the average roughness level of the composite surfaces, which hinders the acquisition of highly consistent data. In-situ scanning probe microscopy (SPM) imaging of the nano-scratch surface area of the samples, reported in the next subsection, confirms this hypothesis. In other words, the depiction of superficial mechanical features of the nanocomposite sample also serves as an evaluation of its surface homogeneity concerning the nanomechanical behavior revealed by XPM investigation.



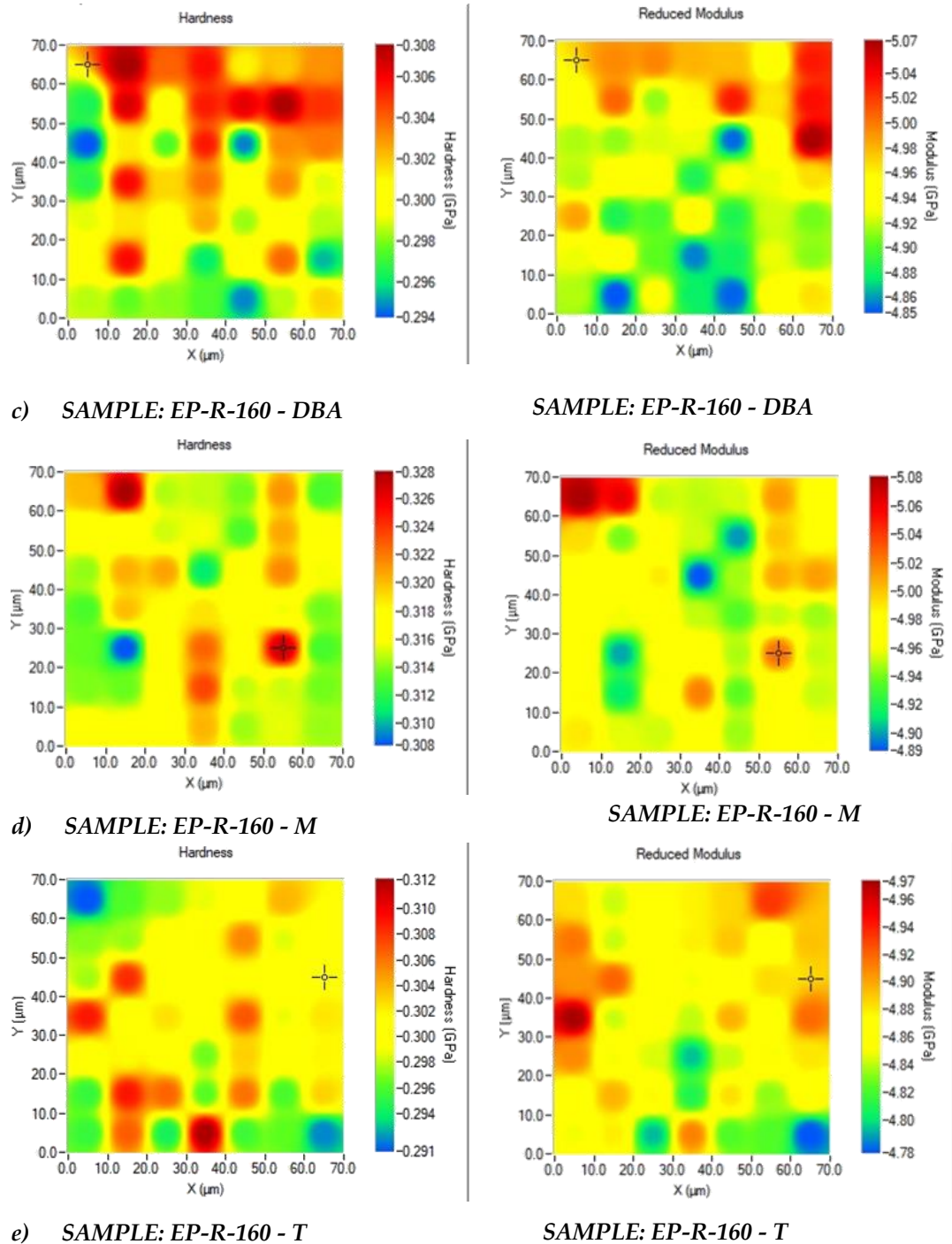
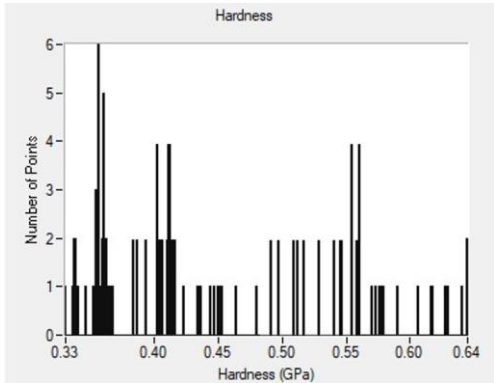
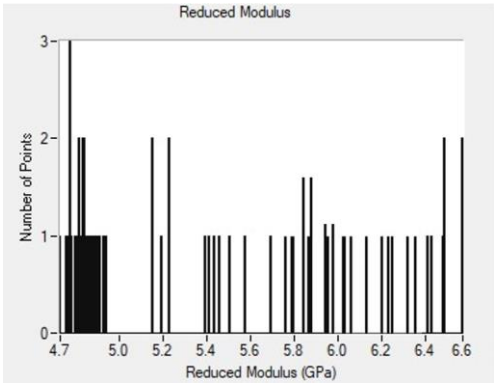


**Figure 12.** XPM plots of a) EP-R; b) EP-R-160; c) EP-R-160-DBA; d) EP-R-160-M, and e) EP-R-160-T samples.

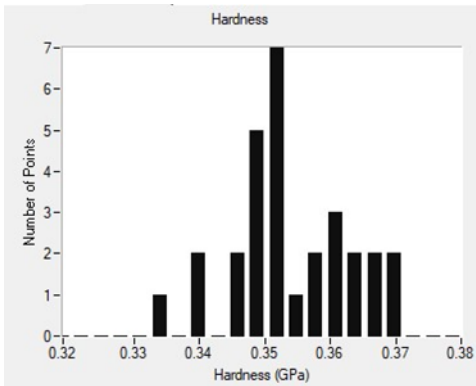
The histogram distribution of nanomechanical parameters for each XPM plot is shown in Figure 13. A weak dispersion of the lines corresponding to hardness and reduced elastic modulus is observed for all investigated samples. This observation is consistent with the nanomechanical XPM plots illustrated in Figure 12. Furthermore, histogram analysis from XPM still shows a good dispersion of rubber domains within the polymer structure. This validates the reliability of the preparation method employed in the present study, considering the tendency of rubber to agglomerate [27], which could result in an imbalanced morphological structure of the composite material.



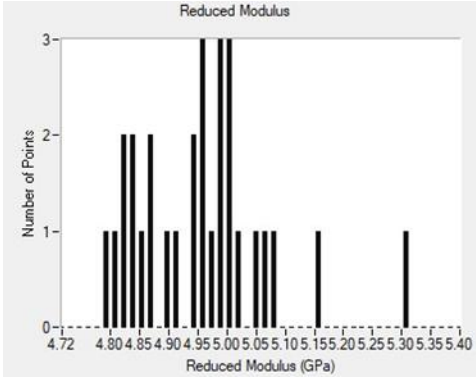
a) SAMPLE: EP



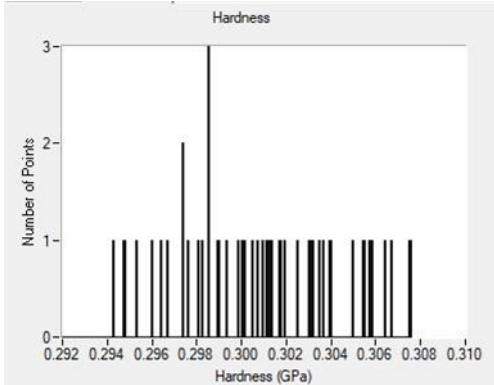
SAMPLE: EP



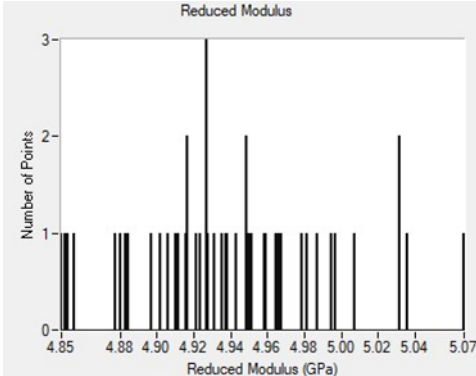
b) SAMPLE: EP-R-160



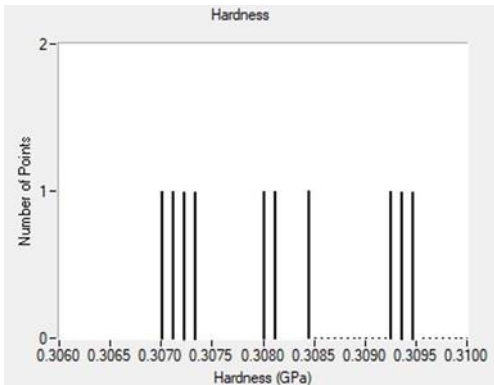
SAMPLE: EP-R-160



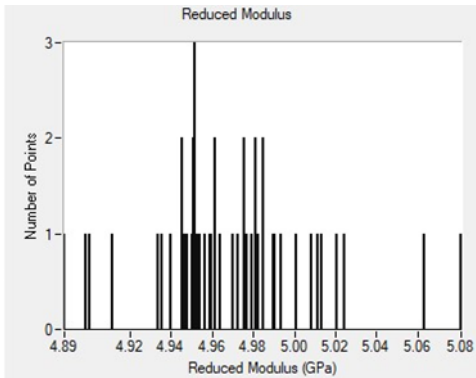
c) SAMPLE: EP-R-160 - DBA



SAMPLE: EP-R-160 - DBA



d) SAMPLE: EP-R-160 - M



SAMPLE: EP-R-160 - M

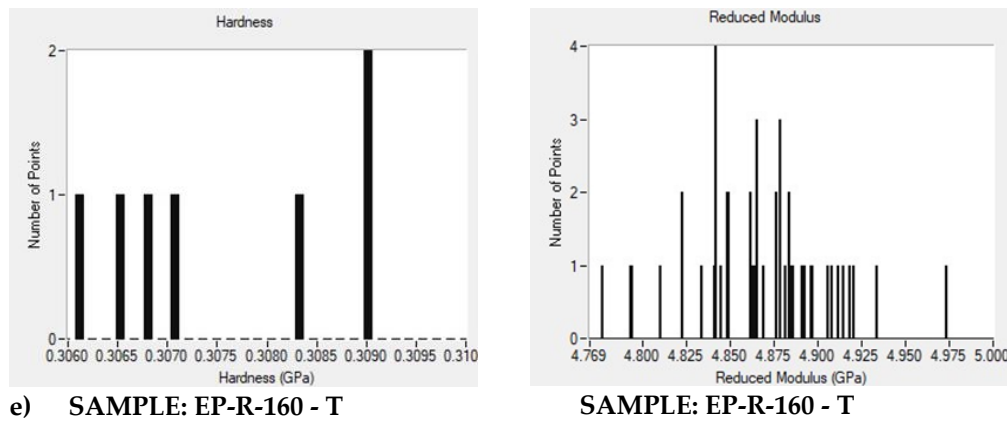


**Figure 13.** XPM histogram plots of a) EP; b) EP-R; c) EP-R-160-DBA; d) EP-R-160-M, e) EP-R-160-T samples.

### 3.4. In-Situ Scanning Probe Microscopy (SPM) Inspection

In-situ scanning probe microscopy (SPM) integrates nanomechanical testing with high-resolution imaging using a single probe, improving accuracy, repeatability, and efficiency. Unlike ex-situ methods, it avoids the need to relocate the sample, thereby saving time and enhancing positioning accuracy.

Concerning the foregoing, Figure 14 (a-e) shows 2D SPM images (left part) and 3D SPM images (right part) of the XPM nanoindentation test trace made on the surface of all samples taken into consideration in our work.

Observing mainly Figure 14 a) related to the not-modified epoxy resin (EP sample), it is possible to confirm previous considerations about the surface smoothness and its quality. Rubber-functionalized epoxy resin displays visible imperfections and irregularities and a not-uniform surface finish. These observations support the statements reported in the previous section concerning the XPM analysis, which has shown better uniform surface color maps for the not-modified epoxy, compared to the other samples.

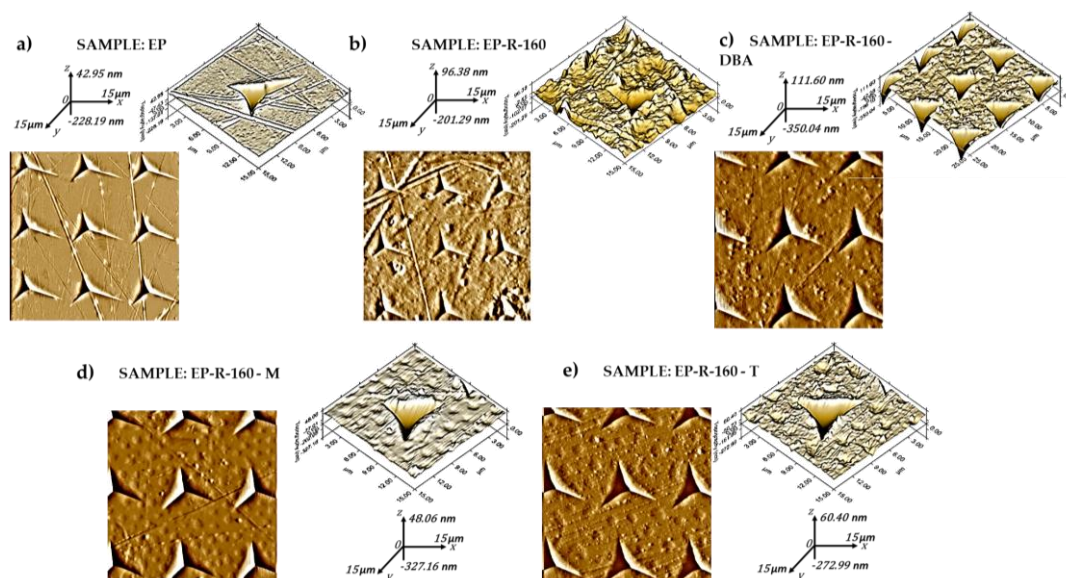


**Figure 14. (a-e).** 2D SPM images of XPM (left parts) and 3D SPM images of XPM (right parts) of nanoindentation test trace made on the surface of a) EP-R; b) EP-R-160; c) EP-R-160-DBA; d) EP-R-160-M, e) EP-R-160-T and e) samples.



Another peculiar aspect which provides information on the nano-scratch behavior of composite materials is the trace profile of the groove left by the indenter tip, as depicted in 2D view (up part) and 3D view (down part) of Figure 15 for the sample EP, EP-R-160 DBA and EP-R-160 - T in a), b) and c), respectively.

The scratch appears noticeably more linear in the case of the unmodified resin (EP sample, see Figure 15 a)). Conversely, for the other two formulations compared (EP-R-160 DBA, see Figure 15 b) and EP-R-160-T, see Figure 15 c)), the path of the indenter tip appears hindered by the rubbery domains, resulting in jagged and less defined scratch outlines. There is also a perceptible difference in the width of the incision, which can be correlated with the deeper notch made by the probe.

These graphical results agree with the lower scratch resistance of these rubber functionalized-based samples, which was discussed in terms of the coefficient of friction in the previous sub-section 3.2. Quasi-static nano-indentation.

Furthermore, from the 3D views of Figure 15 a), b) and c), it is possible to observe the depth of the tip's incision, which in the case of EP sample is lower compared to the other two formulations (EP-R-160-DBA and EP-R-160-T) considered for this comparison via images. This result is consistent with the contact depth values already observed and discussed for these specimens.

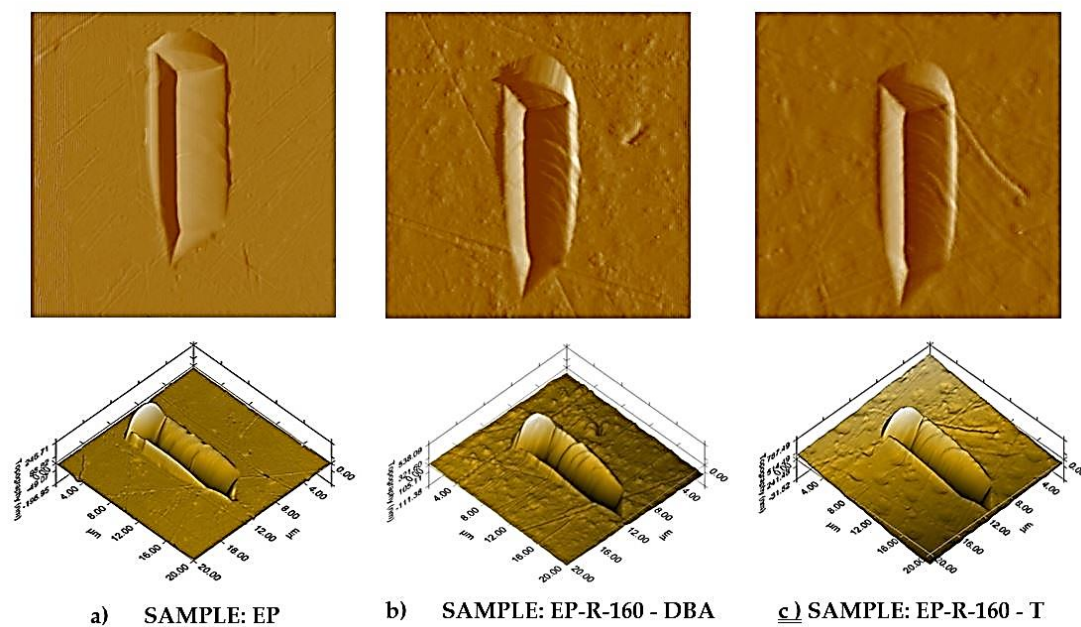


**Figure 15. (a-c).** 2D SPM images (first row) and 3D SPM images (second row) of nano-scratch trace scanned over a  $20\ \mu\text{m} \times 20\ \mu\text{m}$  surface area of: a) EP-R; b) EP-R-160-DBA; c) EP-R-160-T samples.

### 3.5. Multithysics Simulation Study: Results

Finite Element (FE) simulation is a well-recognized technique for analyzing the material's mechanical behavior. Therefore, an experimental-simulation approach is adopted to compare simulation and experimental data. Once the FE model had been validated, it was used to investigate further mechanical properties.

The simulations are conducted focusing exclusively on two materials, EP and EP-R-160-T, which, based on the observed experimental results, are the two most mechanically distinct formulations. The numerical analysis begins with a preliminary investigation over the entire time interval in which the load is applied, aiming to identify the most significant time points for further numerical insights.

Figure 16 reports the z-axis displacement versus the entire time interval (loading, holding, unloading) for EP sample in a) and EP-R-160-T sample in b). The curves provide detailed insights into the material's mechanical behavior during the nanoindentation test. At the beginning of this characterization, as the indenter applies force, the penetration depth increases steadily in linear

mode. This initial loading stage is pivotal for comprehending the material's reaction to mechanical strain. Subsequently, there is a holding period during which the load is maintained. This allows for the observation of any viscoelastic behavior or time-dependent deformation of the material. Finally, during the unloading phase, the applied load is removed, and the indenter retreats from the material. The depth rate profile in this phase reveals significant details about the material's elastic recovery and residual indentation depth.

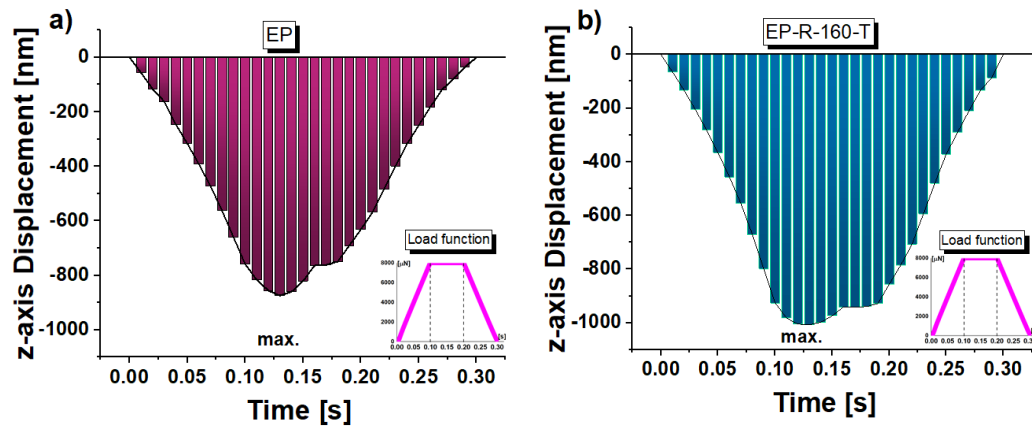


**Figure 16.** z-axis displacement versus the entire time interval for the EP sample in a) and the EP-R-160-T sample in b).

Henceforth, based on the mechanical response over time observed in the previous figure, only some specific time points will be considered as references. More specifically, as indicated in Figure 17 a), three instances (0.025 s, 0.05 s, and 0.075 s) were selected during the loading phase, while during the holding interval, the time instance  $t = 0.13$  s was considered, at which the maximum indentation depth was recorded. The corresponding load values are explicitly reported in the figure. Obviously, for the time instances without load ( $t = 0$  and  $t = 0.3$  s), as shown in Figure 17 b), the samples are at rest with the indenter tip just tangent to their upper surfaces.

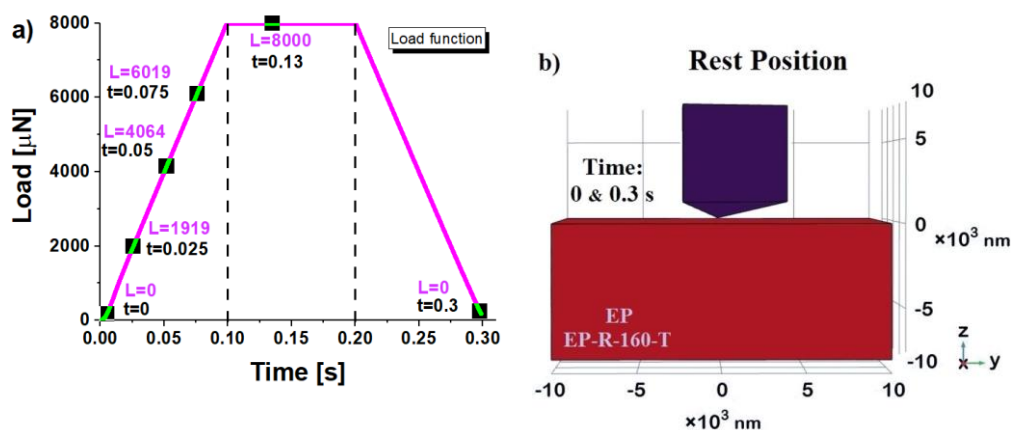


**Figure 17.** Time instances and corresponding loads selected for particular numerical insights in a); resting position ( $t=0$  s and  $t=0.3$  s) with no load ( $L=0$ ) for the EP and EP-R-160-T samples in b).

Figure 18 reports the simulation findings on the z-axis displacement observed for the EP (left part) and EP-R-160-T (right part) for the three-time instances selected during the holding phase, i.e. 0.025s, 0.5s and 0.075 in a), b) and c), respectively. These views allow us to highlight that, consistent with the results of the previous Figure and regardless of the sample, the indentation tip, or equivalently the contact depth, progressively increases over time. In particular, this depth is greater (please refer to the color bar or to the quote lines drawn as guidelines for the eyes) for the EP-R-160-

T sample due to its lower hardness and reduced modulus, which have experimentally determined and already been discussed as results.

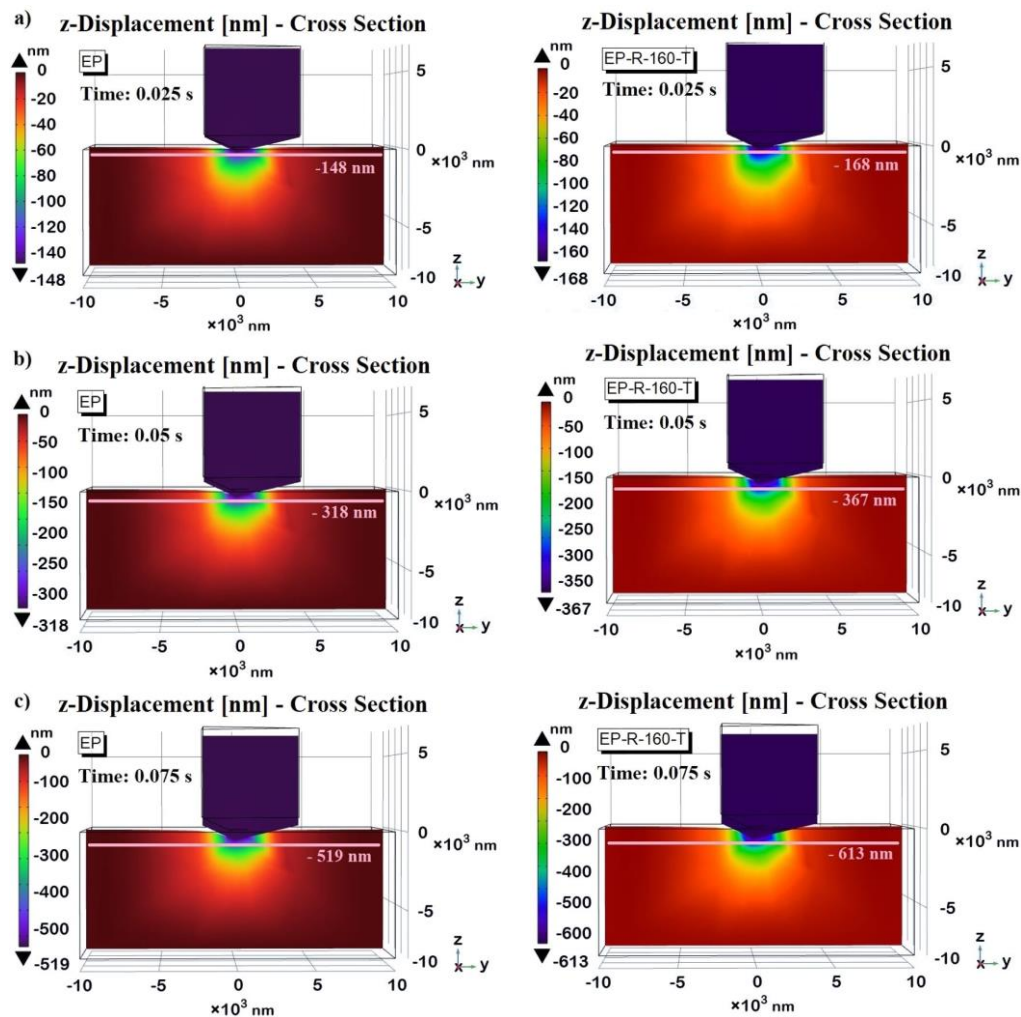


**Figure 18.** Contact depth for EP sample (left) and EP-R-160-T (right) at some selected time instances during the holding phase:  $t=0.025$  s in a),  $t=0.05$  s in b) and  $t=0.075$  s in c).

The time instant  $t=0.13$  s is considered in Figure 19 a) and b) for the EP and EP-R-160-T samples, respectively. At this instant, the maximum contact depth is recorded, measuring -877 nm and -1010 nm for the two samples, which are close to the experimentally obtained results. This particular cross-sectional view allows for a better exploration of the nanoindentation profile. Specifically, the contour lines highlight the greater depth for the EP-R-160-T sample compared to the EP reference according to their hardness values. For the unmodified resin (EP), the z-displacement during nanoindentation is consistently lower. This is because it exhibits higher hardness and stiffness. As the indenter penetrates the surface, the material resists deformation, resulting in a smaller indentation depth. This behavior indicates that the material can withstand higher loads without undergoing significant plastic deformation. In contrast, the sample EP-R-160-T tends to exhibit a greater z-displacement under the same indentation load, reflecting its softer nature. This increased z-displacement is fully compatible with the lower hardness compared to the reference EP. These differences are essential for tailoring materials to specific applications where a balance between hardness and toughness is required.

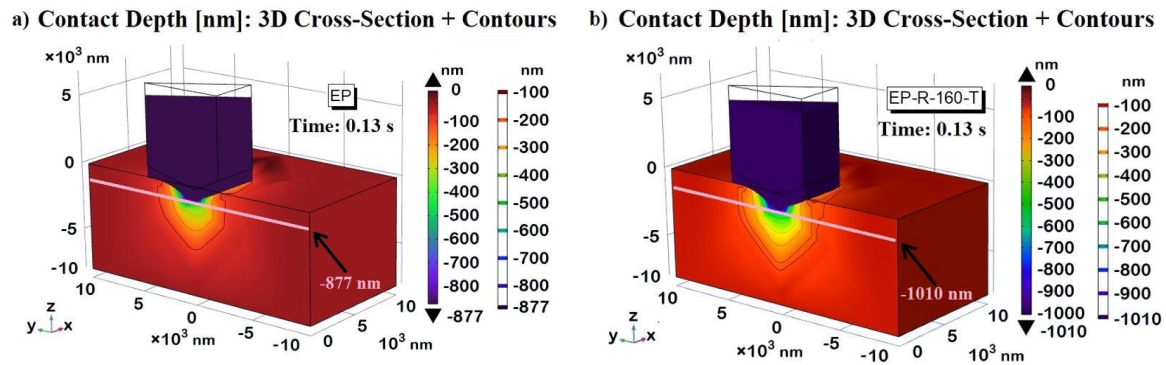


**Figure 19.** Contact depth for EP sample (a) and EP-R-160-T (b) at time instances  $t=0.13$  s at which the maximum contact depth is recorded. The contour lines highlight the different indentation profiles.

The z-axis displacement ( $D$ ) versus time (depth rate) describes the change in penetration depth of the indenter over time. Once again, this parameter is related to the material's mechanical properties and, in particular, to its hardness. Figure 20 reports the results concerning the depth rate of the two considered samples evaluated as the slope of the fitting curve (linear fit,  $R^2$  strictly close to 1) of the displacements of the indenter recording during the loading phase. The EP sample, characterized by a higher hardness compared to the EP-R-10-T, exhibits greater resistance to indenter penetration, and therefore its depth rate is notably lower: the calculated slopes result in 172.7 and 203.8, respectively, for the two samples.

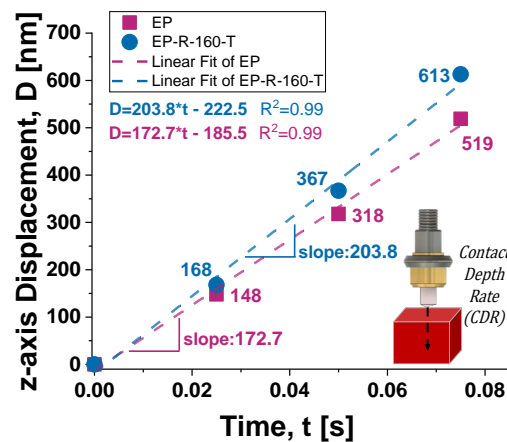


**Figure 20.** z-axis displacement over time, during the loading phase, to evaluate the depth rate of the samples.

In a nanomechanical test of a composite material, the z-axis displacement versus thickness can provide information on the deformation behavior of the material under an applied load. More in detail, as the thickness of the material varies, the z-axis displacement measures the vertical displacement of the material's surface in response to the applied force. This relationship is strictly close to the mechanical properties of materials such as its hardness, elasticity, and resistance to deformation. Figure 21 shows, for the specific time instants considered in this numerical analysis, the z-axis displacement vs the thickness (alongside the segment highlighted in the inset of the same figure) for EP and EP-R-160-T samples, in a) and b), respectively.

As expected, EP, being a stiffer material, exhibits less displacement for a given applied load, resulting in a smaller z-axis displacement versus thickness curve. Conversely, the EP-R-160-T exhibits greater displacement, resulting in a larger curve since it is a softer material.



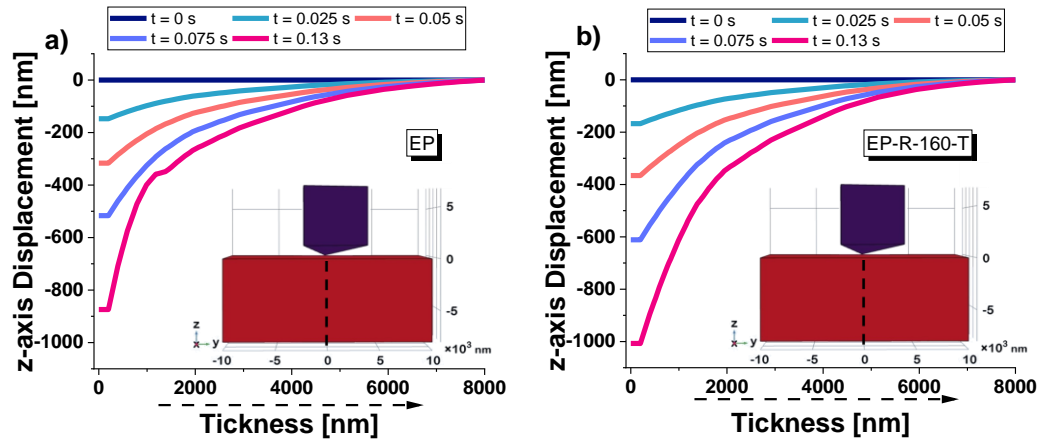


**Figure 21.** z-axis displacement versus thickness, at some selected instants of time, for a) EP-R and b) EP-R-160-T samples.

Figure 22 shows a 3D view of the indentation imprint at the maximum contact depth ( $h_i$ ), i.e., 877 nm and 1010 nm, for the EP sample and the EP-R-160-T sample in a) and b), respectively, whereas the corresponding 2D top views are shown in Figure 22 c) and d). As expected and evident from the analysis of the figures, the projected areas are different according to the relationship  $A_{proj} = f(h_i)$ . With the greater contact depth reached by the tip in the EP-R-160-T sample, its area is significantly larger than that of the EP sample.

Using equation 4, the numerically estimated area values are  $A_{proj}(EP) = 18.89 \mu\text{m}^2$  and  $A_{proj}(EP-R-160-T) = 25.05 \mu\text{m}^2$ , respectively.

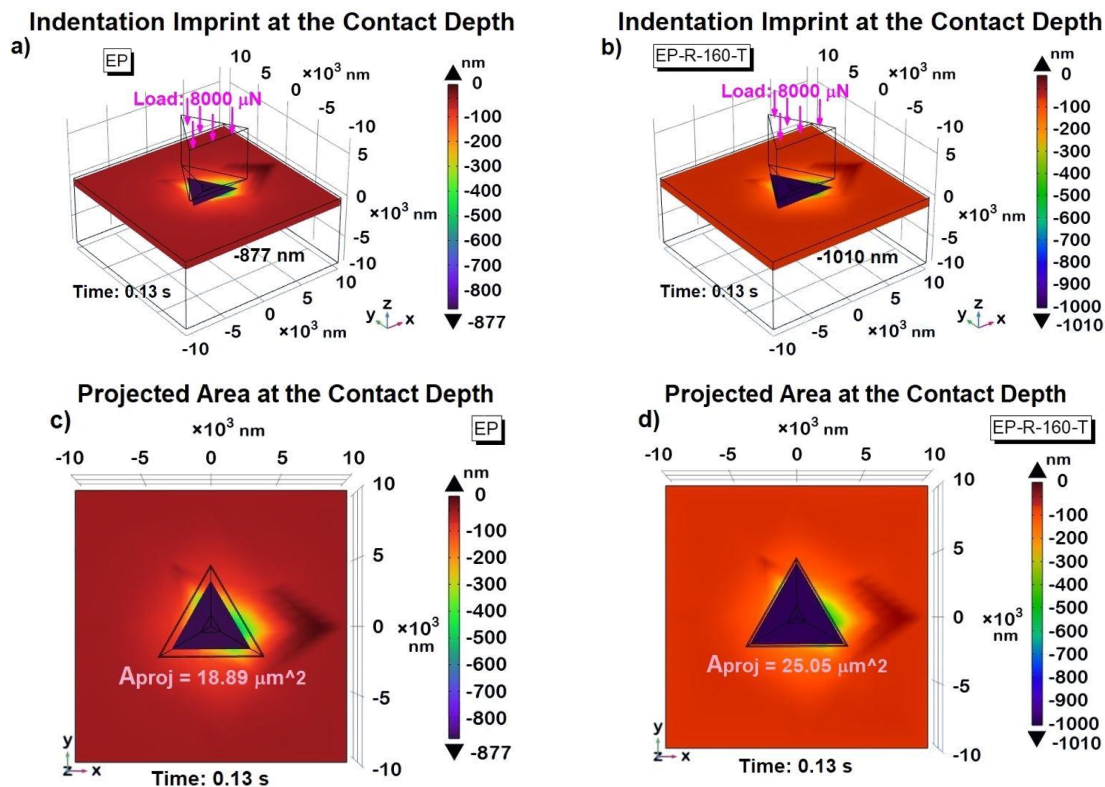


**Figure 22.** Indentation imprint at maximum contact depth for assessing projected areas ( $A_{proj}$ ). 3D-view in a) and b) for EP and EP-R-160-T sample and corresponding 2D top view in 2D view in c) and d).

Once these values were determined and with the maximum applied load (8000  $\mu\text{N}$ ) known, the hardness ( $H$ ) of the materials was calculated using Equation 5. The resulting values were 0.42 GPa for EP and 0.32 GPa for EP-R-160-T, closely matching the experimentally obtained values. These numerical results are summarized and compared with the experimental data in Table 1, showing the percentage variation between the two data sets.

**Table 1.** Comparison of experimental/simulation results for the FE model validation.

SAMPLE:	Contact Depth Exp.	Contact Depth Simul.	Percent Change	Hardness Exp.	Hardness Simul.	Percent Change
EP	876.1 [nm]	877 [nm]	0.103	0.41 [GPa]	0.42[GPa]	2.439
EP-R-160-T	1008.8 [nm]	1010 [nm]	0.119	0.30 [GPa]	0.32 [GPa]	6.667

In nanoindentation investigation, when comparing different composite materials, the displacement magnitude provides further insights into their mechanical properties due to their hardness, elasticity, plasticity, and contact depth differences. Figure 23 shows the deformation contours, detected at the instant  $t=0.13$  s corresponding to the maximum load of 8000  $\mu\text{N}$ , for the EP sample in a) and EP-R-160-T in b). The 3- dimensional cross-sectional views are chosen to provide more detail of the resulting indentation profile.

Regardless of the sample, the deformations are highly localized at the contact area between the material/indenter tip interface and along its periphery. It progressively extends into the bulk of the samples, primarily along the z-axis direction, where the load is applied. The maximum values recorded in both cases (993 nm for EP and 869 nm for EP-R-160-T, respectively) are consistent with the previously presented and discussed contact depth data and hardness values. For the EP sample, being more rigid and thus more prone to crack propagation, it is evident that the deformations extend more significantly in other spatial directions compared to the EP-R-160-T sample. The latter, being relatively softer, better absorbs and dissipates the mechanical energy, reducing the extent of deformations.

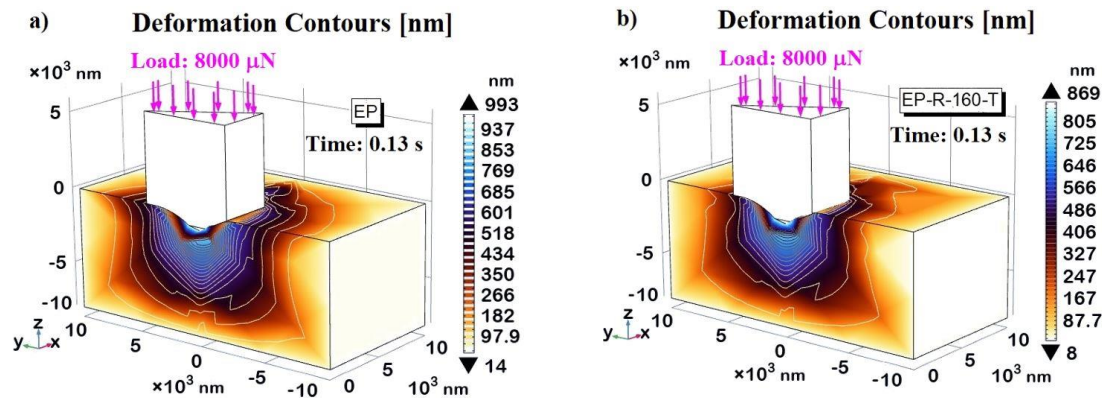


**Figure 23. (a-c).** Deformation contours for EP-R and EP-R-160-T samples, in a) and b), respectively.

Once the model is validated with experimental data and the reliability of the results is confirmed, it can be used to investigate additional mechanical properties that have not yet been here observed experimentally.

For example, in this study, the Von Mises stress is numerically investigated since it is a critical measure in engineering and materials science, particularly for predicting when a material will yield under complex loading conditions. It is especially relevant for composite materials, which combine two or more distinct phases to achieve superior mechanical properties compared to the individual components.

Figure 24 depicts the variation of Von Mises stress (average values) across the total time span of force application (loading, holding, and unloading phases) for both composites, EP and EP-R-160-T, analyzed over the entire domain and on their upper surfaces (see the inserts of the same figure), in a) and b), respectively.

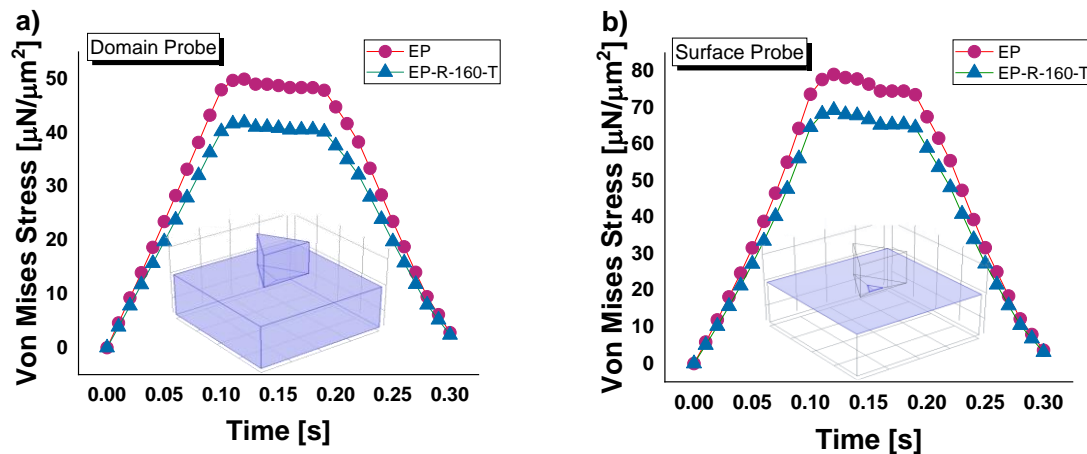


**Figure 24.** Von Mises stress (average value) for EP-R and EP-R-160-T samples, evaluated on the entire domain in a) and upper surfaces of the samples in b), respectively.

From the analysis of these results, it is evident that, regardless of the exploration area, whether volumetric domain or surface, the Von Mises stress remains higher for the EP sample than the EP-R-160-T sample. The maximum stress peak for both samples is reached at  $t=0.13$  s, corresponding to the maximum penetration depth. Therefore, this particular time instant will be considered for the next investigations. These maximum stress peaks are  $49.9 \mu\text{N}/\mu\text{m}^2$  and  $41.8 \mu\text{N}/\mu\text{m}^2$  over the domain for EP and EP-R-160-T, respectively, and  $79.1 \mu\text{N}/\mu\text{m}^2$  and  $69.3 \mu\text{N}/\mu\text{m}^2$  on their upper surfaces.

Figure 25, panels a) and b), respectively, presents a 3D view of the two samples properly sectioned to better visualize the spatial distribution of Von Mises stress.

The pictures highlight that the main stress values are highly localized at the interface indenter probe/contact surface and near its periphery to extend into the surrounding space progressively. In accordance with the results and considerations already reported in the previous Figure 24 a), the higher stress intensity for the EP sample is visually noticeable compared to that of the EP-R-160-T.

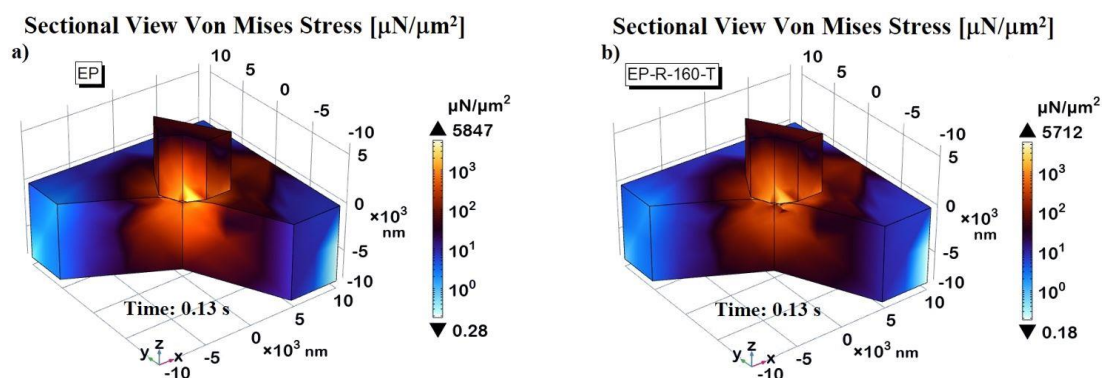


**Figure 25.** 3D-sectional view of Von Mises stress recorded at the time instant  $t=0.13$  s for EP-R and EP-R-160-T in a) and b), respectively.

Finally, the Von Mises stress profiles detected on the upper surfaces of the materials are further analyzed graphically, with 3D views and top views, in Figure 26a) and b) correspondingly for the EP and EP-R-160-T samples. These additional graphical representations again highlight and quantify (see the respective color bars) how the higher Von Mises stress is concentrated in the indentation area.

The traced contour lines provide information on the Von Mises stress distribution on the material surfaces: the appreciable reduced extent exhibited by the EP-R-160-T sample confirms its

facilitated energy dissipation and improved ability to absorb impacts, contributing to the overall toughness and resistance to mechanical stresses.

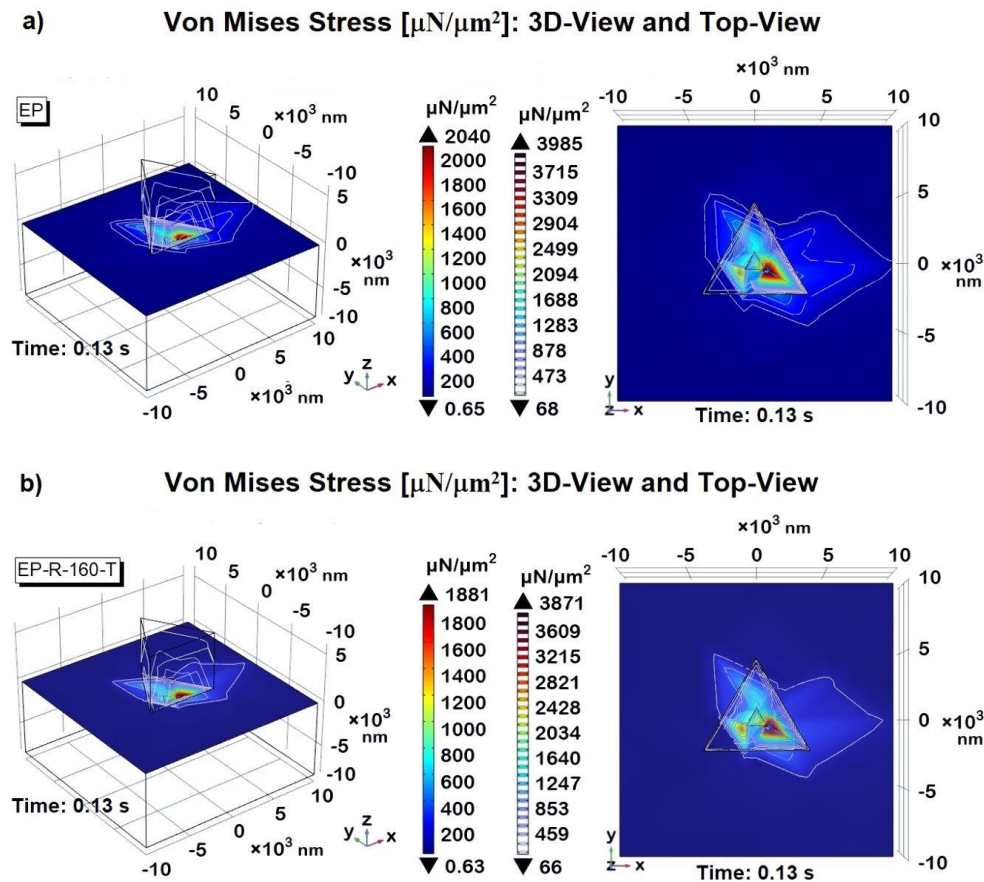


**Figure 26.** Von Mises stress recorded at the time instant  $t=0.13$  s for EP-R and EP-R-160-T in a 3d-view and top-view in a) and b), respectively.

#### 4. Discussions

Nanomechanical testing is currently recognized as a valuable technique used to characterize the mechanical behavior of materials at the nanoscale. In particular, when applied to composite materials, it provides crucial insights into their mechanical properties such as integrity, strength, stiffness, toughness, etc. The results are valuable feedback for optimizing composite material formulations and processing techniques. Among the various approaches for nanomechanical characterization, experimental nanoindentation and nanoscratch testing are performed in the present study. More specifically, nanoindentation tests are widely indicated to measure the hardness, reduced modulus, and contact depth of materials at the nanoscale. In the field of composites, it helps assess the mechanical properties of the hosting matrix and the influence on it of any functionalizing agents or dispersed phases. By performing nanoindentation tests across different regions of the composite, researchers can evaluate the homogeneity of the material. Additionally, nanoscratch testing investigates materials' adhesion and wear resistance at the nanoscale. This technique can assess the interface strength between the matrix and its constituents for composite materials.

In our study, the reported result concerning the higher hardness of sample EP (approximately 36.7% more) compared to the values measured for rubber-functionalized epoxy samples EP-R-160-DBA and EP-R-160-T) can be explained on the basis of several factors. First of all, it must be considered that pure epoxy resins usually have a higher crosslinking density compared to rubber-functionalized epoxy. Crosslinking density refers to the number of chemical bonds connecting polymer chains within the material. Higher crosslinking density leads to a more tightly bound network structure, increasing hardness. This rigidity contributes to the hardness of the material. The



addition of rubber to the epoxy matrix introduces flexible segments within the material, which can disrupt the uniformity of the crosslinked network. The rubber phase tends to act as a plasticizer, reducing the overall rigidity and hardness of the composite material. Moreover, rubber-functionalized epoxy typically exhibits a more dispersed microstructure, with regions of rubber dispersed within the epoxy matrix. These dispersed rubber domains can act as regions of localized deformation under load, reducing the overall hardness of the material, as also evidenced by DMA investigation.

The same considerations just mentioned justify the result regarding the higher value of reduced modulus for the EP sample (about 7% more) compared to all others investigated and the minor contact depth (only 876.1 nm compared to the 1008.8 measured for the EP-R-160-T sample.) associated instead with its resistance to the indentation probe penetration due to the higher hardness value.

In brief, the unmodified resin shows higher hardness and reduced modulus values, while the rubber-functionalized resins display enhanced toughness and energy absorption capabilities due to their limited values of these two mechanical properties.

Conversely, regarding the scratch coefficient of friction, the EP sample exhibits a value of 0.414, which is 11.4% less than the maximum value of 0.461 observed for the EP-R-160-T sample. In rubber-functionalized epoxy, the dispersed rubber phase is relevant in improving the material's scratch resistance and toughness. When a scratch occurs on the surface, the rubber domains within the epoxy matrix serve as energy-dissipating regions. As a result, when the scratching force is applied, the rubber domains can deform and absorb a considerable amount of the energy, thereby reducing the severity of the scratch. This energy absorption mechanism favors the distribution of the applied force more evenly across the material's surface, preventing localized damage and minimizing the risk of crack formation and its subsequent propagation. In brief, the dispersed rubber phase in the host epoxy matrix enhances its ability to withstand mechanical stresses, providing superior scratch resistance and toughness compared to the unmodified resin.

For a comprehensive understanding of the mechanical behavior of multiphase materials, such as those examined in this study, it is crucial to ascertain the mechanical properties of individual phases and their mutual interactions at the nano- and microscale. Recent progress in nanoindentation methodologies has notably minimized testing durations and the XPM (also known as rapid indentation), in conjunction with high-resolution microscopy results, is currently recognized as a valid and fast technique enabling the visualization of hardness and modulus color distribution across a predefined test area of the sample. In brief, XPM expands upon the traditional single indentation approach by employing a piezo scanner to switch positions, transforming it into a grid-like process rapidly. The primary advantage of using the XPM technique lies in its ability to extract valuable insights from nanoindentation of multiphase polymeric materials enabling the generation of contour maps for the composite sample. In the present study, this technique was applied to assess these two mechanical properties visually and to extract valuable information regarding the surface quality of the prepared samples. Although all composites exhibit fairly acceptable surfaces free of significant defects, confirming the optimal choice of chemical composition and production process by the authors, an almost uniform and accurate surface is particularly observed for the EP sample.

Our prepared composites do not necessitate further surface finishing or post-processing to achieve the desired surface quality. This result is highlighted by the SPM analysis performed to complement this nanomechanical characterization. Let us point out that in-situ scanning probe microscopy (SPM) imaging seamlessly integrates nanomechanical investigation with high-resolution SPM imaging. This technique employs a single probe for both imaging the sample surface and conducting the test, enabling quick on-site image acquisition without relocating the sample. This technical solution enhances testing accuracy, repeatability, and efficiency compared to ex-situ imaging methods, which require an additional module like atomic force microscopy (AFM). This translates into increased time required for relocating the sample for imaging and accuracy problems in positioning it on the desired inspection areas.

In a future work, the experimental characterization will be completed with a nanodynamic mechanical testing which can be performed with the same tribo-indenter used and described in the current work.

The study concludes by presenting numerical results obtained through multiphysics simulations conducted with finite element-based software (COMSOL Multiphysics®). In fact, it is widely recognized simulation studies play a crucial role in understanding the mechanical properties of composite materials, especially at the nanoscale. Conducting experimental tests on composite materials can be time-consuming, labor-intensive, and expensive. Simulation studies offer a cost-effective alternative by allowing researchers to explore various design possibilities and hypotheses before manufacturing the composite and experimental testing.

The first step was to ensure the reliability of the numerical results. They were compared with experimental data for validation. In particular, the experimental/simulated results regarding the contact depth and hardness of two reference composites, EP and EP-R-160-T, were compared by finding that the values are in perfect agreement. These two composites were selected based on the experimental characterization; as having mechanically less similar properties, and therefore, they were extensively investigated numerically. In addition to the mechanical properties experimentally analyzed, further properties were investigated with the validated simulation model. In the present study, reserving the investigation of further aspects for a future paper, the attention has been focused on a fundamental property when discussing mechanical properties: the Von Mises stress.

It is often used in engineering and materials science to predict the mechanical behavior of materials under complex loading conditions.

In agreement with the experimental finding, the simulation study confirms that the EP sample with higher hardness and reduced modulus shows less penetration depth under the same applied load. A value of 877 nm (close to the experimental result of 876.1 nm) and 1010 nm (close to the experimental result of 1008.8 nm) were calculated for EP and EP-R-160-T, respectively. The numerical results of the hardness provide a value of 0.42 GPa and 0.32 GPa for EP and EP-R-160-T, respectively, which match the experimental data of 0.41 GPa and 0.30 GPa.

Once again, it is found that the EP sample, given its higher hardness value, is characterized by a more rigid network structure that resists deformation under load, thereby limiting the penetration depth of the indenter. In contrast, the EP-R-160-T sample, due to its compliant behavior, facilitates deeper indentation into the material.

These features strongly affect the Von Mises stress profiles, and, as expected from theory, the EP sample exhibits significantly higher stress levels than the other sample taken for comparison (EP-R-160-T). In conclusion, simulation studies are crucial in composite material design by providing predictive capabilities, optimization opportunities, and detailed insights into material behavior. Utilizing computational modeling enables researchers to expedite materials development, minimize costs, and customize composite materials to suit various application needs.

## 5. Conclusions

This paper mainly focused on investigating the nanomechanical behavior of composites based on the unmodified resin (EP sample) and others, which refer to the same resin functionalized with rubber phase and including molecules able to confer self-healing ability to the epoxy resins. The goal of the work has been to explore the influence of the rubber domains formed within the resin and the presence of self-healing molecules on the overall mechanical features of the resulting structures. More in detail, using an advanced tribo-indenter apparatus, a nanomechanical characterization was performed in terms of hardness, reduced modulus, contact depth, and coefficient of friction. Additionally, to support the experimental activity, a computational approach was developed with commercial software based on the finite element method (FEM) to deepen the observed results and to add knowledge to these advanced materials.

**Supplementary Materials:** The following supporting information can be downloaded at the website of this paper posted on Preprints.org.

**Author Contributions:** Conceptualization G.S., R.G. L.G.; Writing-original draft G.S.; Test samples: E.C.; L.V.; Investigation of mechanical properties E.I. L.V.; Morphological analysis M.R., E.C. and R.L.; Multiphysics Simulation studies: R.G.; Data analysis: G.S. and R.G. M.R.; Writing—review—L.G., and E.I. All authors have read and agreed to the published version of the manuscript.

**Funding:** This research was partially funded by private fund of University “Giustino Fortunato”. The authors also gratefully acknowledge the Prin 2022 project “Integration of Continuous Fibers and Self-healing agents in 3D printed thermoplastic composites (INFINITE)” (Prot. 2022AKTCPh) founded by the Italian Ministry of University and Research, for financial support.

**Institutional Review Board Statement:** Not applicable.

**Data Availability Statement:** Data are contained within the article.

**Conflicts of Interest:** The authors declare no conflicts of interest.

## References

1. Branda, F.; Parida, D.; Pauer, R.; Durante, M.; Gaan, S.; Malucelli, G.; Bifulco, A. Effect of the Coupling Agent (3-Aminopropyl) Triethoxysilane on the Structure and Fire Behavior of Solvent-Free One-Pot Synthesized Silica-Epoxy Nanocomposites. *Polymers (Basel)* **2022**, *14*, 3853, doi:10.3390/POLYM14183853/S1.
2. Bifulco, A.; Marotta, A.; Passaro, J.; Costantini, A.; Cerruti, P.; Gentile, G.; Ambrogio, V.; Malucelli, G.; Branda, F. Thermal and Fire Behavior of a Bio-Based Epoxy/Silica Hybrid Cured with Methyl Nadic Anhydride. *Polymers* **2020**, *Vol. 12*, Page 1661 **2020**, *12*, 1661, doi:10.3390/POLYM12081661.
3. Passaro, J.; Bifulco, A.; Calabrese, E.; Imparato, C.; Raimondo, M.; Pantani, R.; Aronne, A.; Guadagno, L. Hybrid Hemp Particles as Functional Fillers for the Manufacturing of Hydrophobic and Anti-Icing Epoxy Composite Coatings. *ACS Omega* **2023**, *8*, 23596–23606, doi:10.1021/acsomega.3c01415.
4. Righi, C.; Barbieri, F.; Sgarbi, E.; Maistrello, L.; Bertacchini, A.; Andreola, F.N.; D’angelo, A.; Catauro, M.; Barbieri, L. Suitability of Porous Inorganic Materials from Industrial Residues and Bioproducts for Use in Horticulture: A Multidisciplinary Approach. *Applied Sciences* **2022**, *Vol. 12*, Page 5437 **2022**, *12*, 5437, doi:10.3390/APP12115437.
5. Vertuccio, L.; Guadagno, L.; D’Angelo, A.; Viola, V.; Raimondo, M.; Catauro, M. Sol-Gel Synthesis of Caffeic Acid Entrapped in Silica/Polyethylene Glycol Based Organic-Inorganic Hybrids: Drug Delivery and Biological Properties. *Applied Sciences* **2023**, *Vol. 13*, Page 2164 **2023**, *13*, 2164, doi:10.3390/APP13042164.
6. Guadagno, L.; Longo, R.; Aliberti, F.; Lamberti, P.; Tucci, V.; Pantani, R.; Spinelli, G.; Catauro, M.; Vertuccio, L. Role of MWCNTs Loading in Designing Self-Sensing and Self-Heating Structural Elements. *Nanomaterials* **2023**, *Vol. 13*, Page 495 **2023**, *13*, 495, doi:10.3390/NANO13030495.
7. Bohra, B.S.; Singh, P.; Rana, A.; Sharma, H.; Arya, T.; Pathak, M.; Chaurasia, A.; Rana, S.; Sahoo, N.G. Specific Functionalized Graphene Oxide-Based Vitrimers Epoxy Nanocomposites for Self-Healing Applications. *Compos Sci Technol* **2023**, *241*, 110143, doi:10.1016/J.COMPSCITECH.2023.110143.
8. Rana, S.; Solanki, M.; Sahoo, N.G.; Krishnakumar, B. Bio-Vitrimers for Sustainable Circular Bio-Economy. *Polymers (Basel)* **2022**, *14*, doi:10.3390/POLYM14204338.
9. Kanu, N.J.; Gupta, E.; Vates, U.K.; Singh, G.K. Self-Healing Composites: A State-of-the-Art Review. *Compos Part A Appl Sci Manuf* **2019**, *121*, 474–486, doi:10.1016/J.COMPOSITESA.2019.04.012.
10. Islam, S.; Bhat, G. Progress and Challenges in Self-Healing Composite Materials. *Mater Adv* **2021**, *2*, 1896–1926, doi:10.1039/D0MA00873G.
11. Thakur, V.K.; Kessler, M.R. Self-Healing Polymer Nanocomposite Materials: A Review. *Polymer (Guildf)* **2015**, *69*, 369–383, doi:10.1016/J.POLYMER.2015.04.086.

12. Blaiszik, B.J.; Kramer, S.L.B.; Olugebefola, S.C.; Moore, J.S.; Sottos, N.R.; White, S.R. Self-Healing Polymers and Composites. *Annu. Rev. Mater. Res* **2010**, *40*, 179–211, doi:10.1146/annurev-matsci-070909-104532.
13. Li, B.; Cao, P.F.; Saito, T.; Sokolov, A.P. Intrinsically Self-Healing Polymers: From Mechanistic Insight to Current Challenges. *Chem Rev* **2023**, *123*, 701–735, doi:10.1021/ACS.CHEMREV.2C00575/ASSET/IMAGES/LARGE/CR2C00575\_0022.JPEG.
14. Namazi, H. Polymers in Our Daily Life. *Bioimpacts* **2017**, *7*, 73–74, doi:10.15171/BI.2017.09.
15. Mark, J.; Ngai, K.; Graesslev, W.; Mandelkern, L.; Samulski, E.; Wignall, G.; Koenig, J. . . *Physical Properties of Polymers*; 3d Edition.; Cambridge University Press: New York, 2004;
16. Campanella, A.; Döhler, D.; Binder, W.H.; Campanella, A.; Döhler, D.; Binder, H. Self-Healing in Supramolecular Polymers Self-Healing Materials. *Macromol Rapid Commun* **2018**, *39*, 1700739, doi:10.1002/marc.201700739.
17. Utrera-Barrios, S.; Verdejo, R.; López-Manchado, M.A.; Hernández Santana, M. Evolution of Self-Healing Elastomers, from Extrinsic to Combined Intrinsic Mechanisms: A Review. *Mater Horiz* **2020**, *7*, 2882–2902, doi:10.1039/D0MH00535E.
18. White, S.R.; Sottos, N.R.; Geubelle, P.H.; Moore, J.S.; Kessler, M.R.; Sriram, S.R.; Brown, E.N.; Viswanathan, S. Autonomic Healing of Polymer Composites. *Nature* **2001**, *409*, 794–797.
19. Jin, H.; Miller, G.M.; Pety, S.J.; Griffin, A.S.; Stradley, D.S.; Roach, D.; Sottos, N.R.; White, S.R. Fracture Behavior of a Self-Healing, Toughened Epoxy Adhesive. *Int J Adhes Adhes* **2013**, *44*, 157–165, doi:10.1016/J.IJADHADH.2013.02.015.
20. Goyal, M.; Agarwal, S.N.; Bhatnagar, N. A Review on Self-Healing Polymers for Applications in Spacecraft and Construction of Roads. *J Appl Polym Sci* **2022**, *139*, e52816, doi:10.1002/APP.52816.
21. Guadagno, L.; Longo, P.; Raimondo, M.; Naddeo, C.; Mariconda, A.; Sorrentino, A.; Vittoria, V.; Iannuzzo, G.; Russo, S. Cure Behavior and Mechanical Properties of Structural Self-Healing Epoxy Resins. *J Polym Sci Part B: Polym Phys* **2010**, *48*, 2413–2423, doi:10.1002/polb.22139.
22. Outwater, J.O.; Gerry, D.J. On the Fracture Energy, Rehealing Velocity and Refracture Energy of Cast Epoxy Resin. *J Adhes* **1969**, *1*, 290–298, doi:10.1080/00218466908072191.
23. Rahmathullah, M.A.M.; Palmese, G.R. Crack-Healing Behavior of Epoxy-Amine Thermosets. *J Appl Polym Sci* **2009**, *113*, 2191–2201, doi:10.1002/APP.30152.
24. Luo, X.; Mather, P.T. Shape Memory Assisted Self-Healing Coating. *ACS Macro Lett* **2024**, 152–156, doi:10.1021/mz400017x.
25. Nelson, B.A.; King, W.P.; Gall, K. Shape Recovery of Nanoscale Imprints in a Thermoset “Shape Memory” Polymer. *Appl Phys Lett* **2005**, *86*, 1–3, doi:10.1063/1.1868883.
26. Cho, S.H.; White, S.R.; Braun, P. V; Braun, P. V; Institute, B.; Cho, S.H. Self-Healing Polymer Coatings. *Advanced Materials* **2009**, *21*, 645–649, doi:10.1002/ADMA.200802008.
27. Guadagno, L.; Raimondo, M.; Naddeo, C.; Vertuccio, L.; Russo, S.; Iannuzzo, G.; Calabrese, E. Rheological, Thermal and Mechanical Characterization of Toughened Self-Healing Supramolecular Resins, Based on Hydrogen Bonding. *Nanomaterials* **2022**, *12*, 4322, doi:10.3390/NANO12234322/S1.
28. Guadagno, L.; Vertuccio, L.; Naddeo, C.; Calabrese, E.; Barra, G.; Raimondo, M.; Sorrentino, A.; Binder, W.H.; Michael, P.; Rana, S. Reversible Self-Healing Carbon-Based Nanocomposites for Structural Applications. *Polymers (Basel)* **2019**, *11*, doi:10.3390/POLYM11050903.
29. Vertuccio, L.; Calabrese, E.; Raimondo, M.; Catauro, M.; Sorrentino, A.; Naddeo, C.; Longo, R.; Guadagno, L. Effect of Temperature on the Functionalization Process of Structural Self-Healing Epoxy Resin. *Aerospace* **2023**, *10*, 476, doi:10.3390/AEROSPACE10050476.



30. Gibson, R.F. A Review of Recent Research on Nanoindentation of Polymer Composites and Their Constituents. *Compos Sci Technol* **2014**, *105*, 51–65, doi:10.1016/j.COMPSCITECH.2014.09.016.
31. Yan, C.; Bor, B.; Plunkett, A.; Domènech, B.; Maier-Kiener, V.; Giuntini, D. Nanoindentation Creep of Supercrystalline Nanocomposites. *Mater Des* **2023**, *231*, 112000, doi:10.1016/j.matdes.2023.112000.
32. Lam, C.K.; Lau, K.T. Localized Elastic Modulus Distribution of Nanoclay/Epoxy Composites by Using Nanoindentation. *Compos Struct* **2006**, *75*, 553–558, doi:10.1016/j.compstruct.2006.04.045.
33. Karimzadeh, A.; R. Koloor, S.S.; Ayatollahi, M.R.; Bushroa, A.R.; Yahya, M.Y. Assessment of Nano-Indentation Method in Mechanical Characterization of Heterogeneous Nanocomposite Materials Using Experimental and Computational Approaches. *Sci Rep* **2019**, *9*, doi:10.1038/S41598-019-51904-4.
34. Arora, G.; Pathak, H. Nanoindentation Characterization of Polymer Nanocomposites for Elastic and Viscoelastic Properties: Experimental and Mathematical Approach. *Composites Part C: Open Access* **2021**, *4*, doi:10.1016/J.JCOMC.2020.100103.
35. Ramos, V.D.; Da Costa, H.M.; Soares, V.L.P.; Nascimento, R.S.V. Modification of Epoxy Resin: A Comparison of Different Types of Elastomer. *Polym Test* **2005**, *24*, 387–394, doi:10.1016/J.POLYMERTESTING.2004.09.010.
36. Spinelli, G.; Lamberti, P.; Tucci, V.; Kotsilkova, R.; Ivanov, E.; Menseidov, D.; Naddeo, C.; Romano, V.; Guadagno, L.; Adami, R.; et al. Nanocarbon/Poly(Lactic) Acid for 3D Printing: Effect of Fillers Content on Electromagnetic and Thermal Properties. *Materials* **2019**, *Vol. 12*, *Page 2369* **2019**, *12*, 2369, doi:10.3390/MA12152369.
37. Guadagno, L.; Aliberti, F.; Longo, R.; Raimondo, M.; Pantani, R.; Sorrentino, A.; Catauro, M.; Vertuccio, L. Electrical Anisotropy Controlled Heating of Acrylonitrile Butadiene Styrene 3D Printed Parts. *Mater Des* **2023**, *225*, 111507, doi:10.1016/J.MATDES.2022.111507.
38. Čech, J.; Haušild, P.; Kovářik, O.; Materna, A. Examination of Berkovich Indenter Tip Bluntness. *Mater Des* **2016**, *109*, 347–353, doi:10.1016/J.MATDES.2016.07.033.
39. Khelifa, M.; Fierro, V.; Celzard, A. Finite Element Simulation of Nanoindentation Tests Using a Macroscopic Computational Model. *Journal of Mechanical Science and Technology* **2014**, *28*, 3209–3217, doi:10.1007/S12206-014-0730-1.
40. Troyon, M.; Huang, L. Correction Factor for Contact Area in Nanoindentation Measurements. *J Mater Res* **2005**, *20*, 610–617, doi:10.1557/JMR.2005.0099.
41. Lee, J.H.; Lee, H.; Kim, D.H. A Numerical Approach to Evaluation of Elastic Modulus Using Conical Indenter with Finite Tip Radius. *J Mater Res* **2008**, *23*, 2528–2537, doi:10.1557/JMR.2008.0314.
42. Doerner, M.F.; Nix, W.D. A Method for Interpreting the Data from Depth-Sensing Indentation Instruments. *J Mater Res* **1986**, *1*, 601–609, doi:10.1557/JMR.1986.0601/METRICS.
43. Oliver, W.C.; Pharr, G.M. Measurement of Hardness and Elastic Modulus by Instrumented Indentation: Advances in Understanding and Refinements to Methodology. *J Mater Res* **2004**, *19*, 3–20.
44. Guadagno, L.; Raimondo, M.; Vertuccio, L.; Lamparelli, E.P.; Ciardulli, M.C.; Longo, P.; Mariconda, A.; Della Porta, G.; Longo, R. Electrospun Membranes Designed for Burst Release of New Gold-Complexes Inducing Apoptosis of Melanoma Cells. *International Journal of Molecular Sciences* **2022**, *Vol. 23*, *Page 7147* **2022**, *23*, 7147, doi:10.3390/IJMS23137147.

45. Sneddon, I.N. The Relation between Load and Penetration in the Axisymmetric Boussinesq Problem for a Punch of Arbitrary Profile. *Int J Eng Sci* **1965**, *3*, 47–57, doi:10.1016/0020-7225(65)90019-4.
46. Němeček, J.; Němeček, J.; Lukeš, J. High-Speed Mechanical Mapping of Blended Cement Pastes and Its Comparison with Standard Modes of Nanoindentation. *Mater Today Commun* **2020**, *23*, doi:10.1016/J.MTCOMM.2019.100806.

**Disclaimer/Publisher's Note:** The statements, opinions and data contained in all publications are solely those of the individual author(s) and contributor(s) and not of MDPI and/or the editor(s). MDPI and/or the editor(s) disclaim responsibility for any injury to people or property resulting from any ideas, methods, instructions or products referred to in the content.